Ben-Gurion University of the Negev
Faculty of Engineering Sciences
Department of **Software and Information Systems Engineering**

Quantifying the dynamics of long-range cell-cell mechanical communication

Thesis submitted in partial fulfillment of the requirements for the Master of Sciences degree

By: Assaf Nahum

September 2020

Ben-Gurion University of the Negev
Faculty of Engineering Sciences
Department of **Software and Information Systems Engineering**

Quantifying the dynamics of long-range cell-cell mechanical communication

Thesis submitted in partial fulfillment of the requirements for the Master of Sciences degree

By: Assaf Nahum

Supervised by: Dr. Assaf Zaritsky

Signature of Author:……….………….………...   Date:………..…18/09/20…….

Signature of Supervisor:……………….…….……   Date:………..…19/09/20…….

Signature of Chairperson of the
Committee for Graduate Studies………..…..………...   Date:………………………….

September 2020

Abstract

Cells sense, manipulate and respond to the mechanical properties of their microenvironment in a plethora of physiological processes, yet whether and how cells interpret environmental cues to communicate with distant cells is mostly unknown. We present a computational method to systematically infer and quantify long-range mechanical cell-cell communication through the extracellular matrix (cell-ECM-cell communication). We found that local ECM remodeling fluctuations in between communicating cells were synchronized due to propagating forces. By correlating these ECM fluctuations, in finite element simulations and live 3D imaging of fibroblasts embedded in fibrin gels, our method matched pairs of communicating cells with high accuracy, and identified whether and to what extent one cell was influenced by its communication partner. Using this method, we revealed that cells actively respond to the mechanical signal that they sense from the other cell, amplifying the formation of a dense fibrin band between the communicating cells. Our method sets the stage to measure the fundamental aspects of intercellular long-range mechanical communication in physiological contextes and may provide a new functional readout for high content 3D image-based screening.

Acknowledgements

Contents

Terminology

Term	Definition
ECM	Extracellular-matrix, a 3D network of fibrous structure supporting the surrounding cells.
Cell-ECM Interaction	The contractile force on the ECM applied by the nearby cell. (Fig. 1B).
Cell-ECM-Cell Communication	Long-range mechanical intercellular communication through the ECM. (Fig. 1B).
Cell Pair	Two simulated or experimental cells that may or may not communicate.
Connecting Axis	The axis defined by the line connecting the cells' centers of a cell pair. (Fig. S1, black).
Z Axis	The axis parallel to the microscopy axial imaging plane and perpendicular to the connecting axis. (Fig. S1, cyan).
XY Axis	The axis perpendicular to the connecting axis and to the Z axis. (Fig. S1, purple).
Band	Remodeled ECM of (increased density of) the fibers along the connecting axis of a cell pair.
Pair Distance	The distance between the cells in a cell pair. (Fig. S3A).
Window Distance	The distance between a cell boundary and it's quantification window. (Fig. S3A).
Inner Correlation	The temporal correlation of quantified ECM remodeling dynamics of windows located in the inner regions along the connecting axis of a cell pair. (Fig. 3A, green).
Outer Correlation	The temporal correlation of quantified ECM remodeling dynamics of windows located in the outer regions along the connecting axis of a cell pair. (Fig. 3A, purple).
Same-versus-different Pair Analysis	The inner correlation between a simulated pair of communicating cells versus the correlation between the inner region of one cell from that pair and the inner region of another cell from a different simulated pair of communicating cells in a different fibrous network. (Fig. 4A).
Fake-static cell pair	A manually defined fake cell pair with fixed coordinates, distant from real cells. (Fig. S13C, shadow-less cyan cells).
Fake-following cell pair	A manually defined fake cell pair with coordinates following its corresponding cell pair motion by shifting in X' and Y' while maintaining a fixed distance from the real pair. (Fig. S13A, cyan cells).
Matchmaking Analysis	The fiber density dynamics of a cell inner region correlated to all other cell's inner region of the cell pairs in the experiment and reporting the rank of its true matching partner. (Fig. 6A).

List of Figures

Lists of tables and videos are presented in the supplementary sections and can be accessed here: https://www.biorxiv.org/content/10.1101/2020.07.30.223149v1.supplementary-material

Introduction

From developmental processes to cancer metastasis, the ability of cells to communicate with one another, over short and long distances, is key for all coordinated cell behaviors. Many mechanisms exist for cell-cell communication, including direct mechanical contacts[1], gap junctions[2], membrane nanotubes that transmit cytoplasmic content via direct cell-cell contact[3], release (exocytosis) and internalization (endocytosis) of diffusive secreted factors or extracellular vesicles[4], or mechanical deformation that propagates through the substrate between cells[5]. Common to all these diverse mechanisms are the following hallmark stages of cell-cell communication: one cell releases a signal that is transmitted to another cell, the second cell receives the signal, processes it, and changes its internal state in response (Fig. 1A). This is essentially a complex dynamic process that is challenging to quantitatively characterize. Here, we focus on long-range mechanical cell-cell communication through the extracellular matrix (ECM) as a model system to systematically study the different stages of cell-cell communication.

Many types of cells apply considerable traction forces on their surrounding matrix leading to ECM-deformations that can propagate to large distances of tens of cell diameters away[5–17]. These deformations can be sensed by distant cells, that in response rearrange their internal molecular state[18] and actively respond[19] (Fig. 1A). This long-range mechanical intercellular communication through the ECM (termed here *cell-ECM-cell communication*) was observed in vivo[18] and in vitro for cells embedded in synthetic[5,6] and biopolymer fibrous matrices[7–16], and are thought to play a key role in tissue regeneration[20–22], fibrosis[19,23,24] and cancer metastasis[8,25,26].

Quantification of mechanical cell-ECM-cell communication has been typically achieved by analyzing the mutual orientation, morphology or functional activity of communicating cell pairs[5,16,27], by measuring the density, alignment or displacement of the remodeled ECM band between the cell pairs[7–9,13,17,28–30]. While these measurements characterize the formation of the fibrous band between communicating cells, they do not provide much information regarding how the mechanical signal propagates from one cell to the other and/or how the cells actively respond to this mechanical signal. This hampers our ability to distinguish which cells are actually communicating from the many cells that have the potential to communicate, limiting the possibility to infer the complex tangle of cell-cell interactions in complicated environments. Bridging this gap will enable tackling long-standing open questions in how tissues develop and

diseases progress by enabling us to identify which cells are communicating with each other, and to what extent, in complex environments.

Cells embedded in physiologically-relevant 3D matrices are an excellent model to study the spatiotemporal dynamics of cell-ECM-cell communication. The ability to perform dual-channel quantitative live imaging, where one channel captures the transmitted signal in the ECM, and the other channel captures the cell state (e.g., cell morphology and/or specific molecular markers) provides a unique setting for following the different steps involved in cell-cell mechanical communication. Here, we developed a new method to quantify the transmitted ECM signal in between communicating cells by correlating temporal fluctuations of the remodeled matrix. Computational simulations and live cell imaging experiments were used to demonstrate the power of our method in quantifying cell-ECM-cell communication and acquiring new insight regarding this mode of intercellular communication.

Results

Analysis of ECM density near single cells and between pairs of communicating cells in simulations and experiments

During cell-cell mechanical communication, every localized fibrous region in between the communicating cells is affected by two components: the contractile force of the nearby cell (referred as 'c*ell-ECM' interaction*), and the force transmitted from the second distant cell (referred as '*cell-ECM-cell' communication*) (Fig. 1B). To quantitatively characterize the independent contribution of each of these two components, we quantified the overall change in the ECM density between pairs of communicating cells and compared it to single cells interacting with the ECM. We combined finite element discrete modeling of contracting cells embedded within 2D fibrous networks and experiments of NIH/3T3 Fibroblast cells embedded in 3D fibrin gels (Methods).

To enable quantitative comparison across experiments and between simulations and experiments, we normalized the fiber density to its z-score - the number of standard deviations away from the mean background fiber density at regions that were not influenced by the cells (Methods). To measure fiber density in between cell pairs in 3D we transformed the microscopy axes to a new 3D coordinate system: the connecting axis, defined by the line connecting the cells' centers; the Z axis, the axis parallel to the microscopy axial imaging plane and perpendicular to the connecting axis; and the XY axis, perpendicular to the connecting axis and to the Z axis (Methods, Fig. S1, Video S1).

In simulations of single contractile cells, we found that the regions next to the cell's boundary became denser following the application of 50% cell contraction. This densification faded to the background level at a characteristic distance of approximately 2 cell diameters (Fig. 1C-D). These simulations were consistent with experimental measurements of fibroblasts embedded in 3D fibrin gels, where fibrin intensity was used as a proxy of fiber density (Fig. 1C-D, Methods).

Upon the presence of a second cell, the overall densification was governed by the integrated contractile activity of both cells (Fig. 1B). This dual contribution led to the formation of a visible band of increased density along the connecting axis between the cells, visually apparent in simulations and in approximately 60% of the imaged cell pairs (Fig. 1E-F, see Fig. S1, Video S1

and Methods for details on 3D visualization and quantification). Bands between pairs of cells were characterized with increased fiber density in relation to single cells (Fig. 1F vs. 1D). Intriguingly, the change between cell-ECM (single cell) and cell-ECM-cell (cell pairs) was more prominent in the experiments in comparison to the simulations (Fig. 1G). This observation of increased density in cell pairs in experiments versus simulations could be explained by the cells actively responding to the mechanical signal transmitted from the communication partner, a process that is not modeled in the simulations. We did not notice a major change in fiber density for pairs at increasing distances (Fig. S2). However, careful analysis revealed that the distance between the pair of communicating cells (termed *pair distance*) was negatively correlated to the density of fibrous regions further away from the cell (termed *window distance*) (Fig. S3), implying stronger mechanical interaction for pairs that are closer to one another (Fig. 1B).

We conclude that the dense fibrous bands between cell pairs are indicative of a mechanical communication mechanism. Notably, the increased fiber density between communicating cells in comparison to the density around a single cell could be used to quantitatively decouple the contribution of the cell-autonomous and cell-cell communication components that together form the visible band between the cells (Fig. 1H). These results establish the potential of analyzing ECM density, in 2D finite element simulations and experiments of fibroblasts embedded in 3D fibrin gels, to study cell-cell communication.
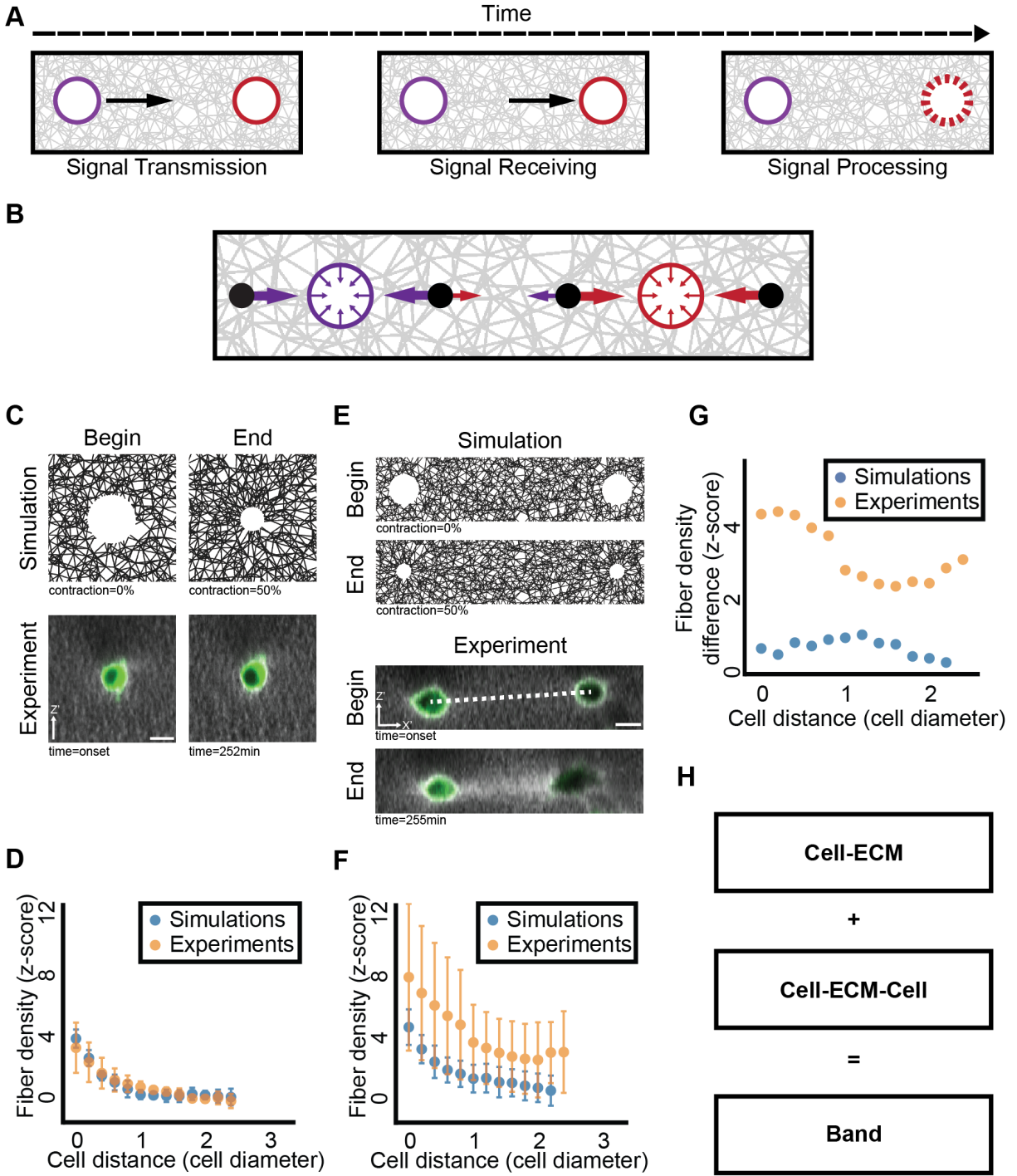
Figure 1: Quantifying ECM densification in cell-ECM interactions and cell-ECM-cell communication. (**A**) Universal hallmarks of cell-cell communication. One cell transmits a signal (left). The signal is received by a second cell (middle). The second cell reacts to the received signal by altering its internal state (right). (**B**) Fibers in between pairs of cells are remodeled by the integrated mechanical forces that both cells exert on the ECM. Colored arrows depict the magnitude of the force experienced in a specific location in the fibrous gel that are generated by the two cells. (**C-D**) Quantifying cell-ECM interactions. (**C**) Representative simulation visualization (top) and experimental images (bottom) at the onset (left) and after (right) 50% cell contraction or 4 hours of cell imaging. Scale bar = 15 μm. (**D**) Quantifying fiber

densification around a single cell in simulations and experiments. N = 7 cells for both simulations and experiments. (**E-F**) Quantifying cell-ECM-cell communication. (**E**) Representative simulation visualization (top) and experimental images (bottom) at the onset (left) and after (right) simulation/imaging correspondingly. Simulated cell contraction was set to 50%, cell imaging time was 255 minutes. The initial distance between simulated cell centers was set to 7 cell diameters, and was ~7.8 cell diameters (~117 μm, assuming mean fibroblast diameter of 15 μm) in imaging. Scale bar = 15 μm. White dashed line in the experimental image represents the connecting axis between the cells. (**F**) Quantifying "band" formation in between cell pairs. N = 20 cell pairs at a distance of 7 cell diameters (simulations). Approximately 60% (36/59) of cell pairs in experiments formed visible "bands" of denser fibers in the connecting axis between the cells. N = 13 cell pairs (experiments) at distances of 6-8 cell diameters (90-120 μm). (**G**) Mean deviation in fiber density between pairs and single cells in simulations and experiments. (**H**) A dense fiber "band" between cell pairs is formed by a combination of cell-ECM interactions and cell-ECM-cell communication. Mean and standard deviation are displayed in all quantitative figure panels.

Positive feedback between fiber density and change in fiber density leads to band formation

Cell-ECM remodeling and the formation of a band between mechanically communicating cells is a dynamic process. To quantitatively characterize this process in our simulations, we consecutively applied 1% cell contraction for 50 steps, reaching 50% cell contraction. For each step, we recorded the fiber density around a cell or between communicating cells. These iterative simulations captured the temporal dynamics of cell-ECM remodeling and cell-ECM-cell communication. Experimentally, 3D confocal live imaging was used to follow the temporal dynamics of single or pairs of fibroblast cells embedded in 3D fibrin gels. As expected, the fiber density close to the cells' edge gradually increased over time in both simulations and experiments, in single cells and in pairs of communicating cells (Fig. 2A-D, Video S2, Video S3, Video S4, Video S5). The denser band at the onset of imaging was attributed to the time (approximately 30 minutes) passed from setting up the experiment until the beginning of imaging (Fig. 2B and Fig. 2D, z-score of approximately 3 standard deviations above the background density).

Intriguingly, simulations revealed a correlation between the fiber density and the change in fiber density between consecutive contraction steps (Fig. 2E). We verified this predicted correlation between fibrin intensity and the change of the intensity in experiments in consecutive (15 minutes) time frames at the first 90 minutes of the experiment (Fig. 2F). At later times this correlation dropped, but was still present (Fig. S4). These results revealed a positive feedback

between fiber density and the change in fiber density that lead to an effective and rapid fiber densification and band formation between mechanically communicating pairs of cells.
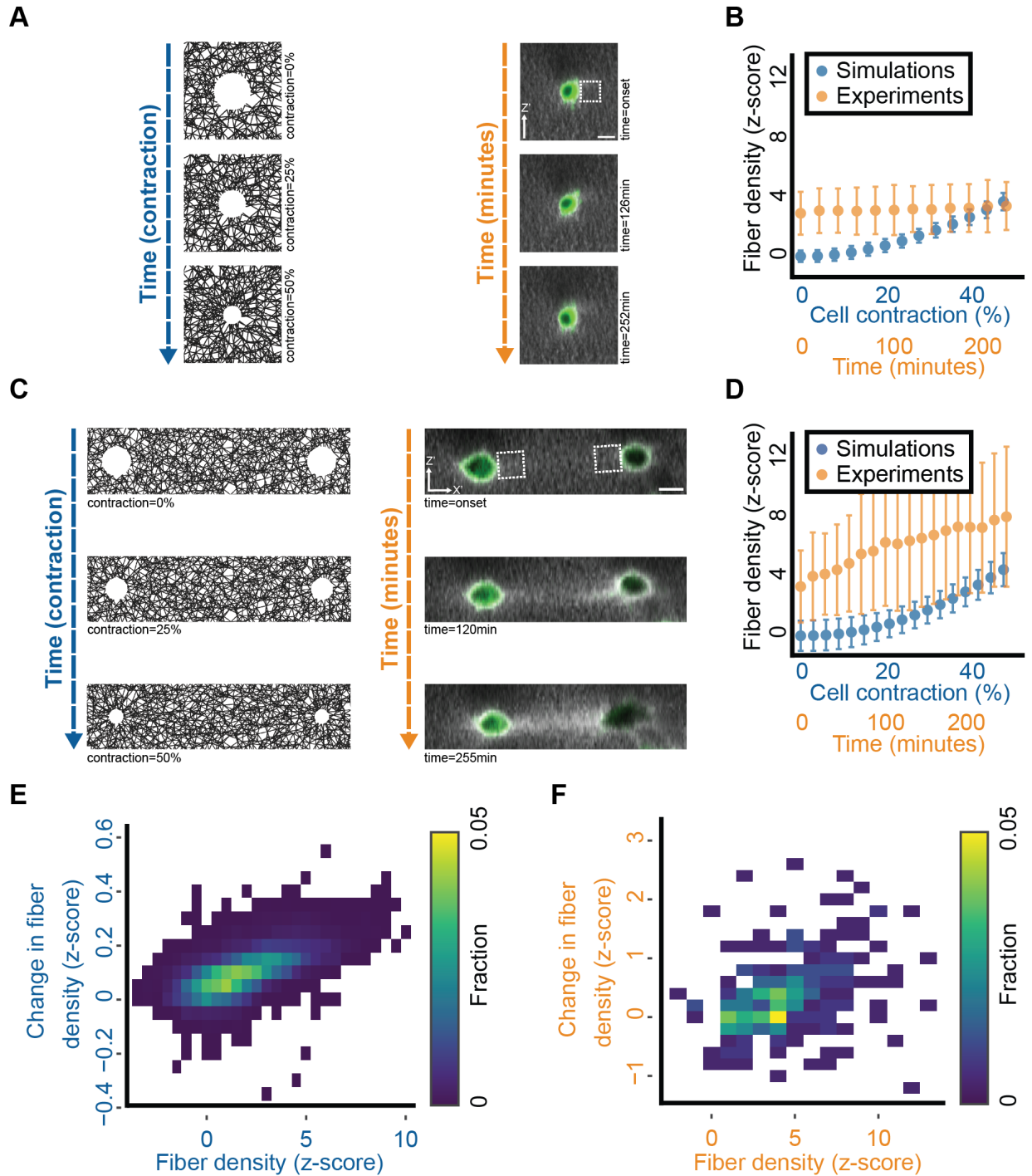
Figure 2: Quantifying the dynamics of ECM densification during cell-ECM interactions and cell-ECM-cell communication. (**A-B**) Quantifying the dynamics of cell-ECM interactions. (**A**) Representative simulation visualization (left) and experimental images (right), at the onset (top), 25% cell contraction or 2 hours of live cell imaging (middle), and 50% cell contraction or 255 minutes of live cell imaging

(bottom). Scale bar = 15 μm. White dashed rectangle next to the cell boundaries represents one quantification window (see Methods for details). (**B**) Quantifying fiber densification dynamics near a single cell in simulation and experiments. N = 7 cells for both simulations and experiments. Experimental setup time explains the denser band at the onset of imaging. (**C-D**) Quantifying cell-ECM-cell communication. (**C**) Representative simulation visualization (left) and experimental images (right) at the onset (top), 25% cell contraction or 2 hours of live cell imaging (middle), and 50% cell contraction or 255 minutes of live cell imaging (bottom). The pair distance between simulated cell centers was set to 7 cell diameters, and was ~7.8 cell diameters (~117 μm, assuming mean fibroblast diameter of 15 μm) in imaging experiments. Scale bar = 15 μm. White dashed rectangles next to cell boundaries represent the quantification window (Methods). (**D**) Quantifying "band" formation in between pairs of cells. N = 20 cell pairs at a pair distance of 7 cell diameters (simulations). N = 13 cell pairs (experiments) at pair distances of 6-8 cell diameters (90-120 μm). (**E-F**) Two-dimensional distribution of fiber density and change in fiber density measured in consecutive contraction steps (simulations) or time frames (experiments). Quantification windows adjacent to each cell along the band. (**E**) Simulations. N = 120 cell pairs (N = 20 for distances of 5, 7, 9, 12, 15 and 17 cell diameters). Constant cell contraction of 1% between consecutive time frames. Pearson correlation coefficient = 0.59, p-value < 0.0001. (**F**) Experiments. N = 30 pairs of cells in distances between 5 and 10.5 cell diameters (75-157.5 μm). Temporal resolution of 15 minutes between consecutive time frames. The first 90 minutes from the onset of imaging was recorded. Pearson correlation coefficient = 0.46, p-value < 0.0001.

Cell contractile heterogeneity is necessary to quantitatively identify simulated cell-ECM-cell communication using temporal correlation of local ECM remodeling dynamics

Given that local ECM regions located along a band experience forces exerted by both cells, we hypothesized that local ECM remodeling dynamics contain sufficient information to distinguish ECM regions located along the band of communicating cells from non-communicating ECM regions. This hypothesis was based on our earlier observation regarding the discrepancy between ECM remodeling by a single and a pair of cells (Fig. 1G) and the temporal process that led to that final remodeling. We expected that the temporal correlation of ECM remodeling dynamics between cell pairs (inner regions adjacent to each cell along the band, termed '*inner correlation*') will exceed that of non-communicating outer regions (outer regions adjacent to each cell at the outskirts of the band, termed '*outer correlation*') (Fig. 3A). In simulations of pairs of communicating cells, we found outer and inner positive correlations using either the fiber density dynamics or its temporal derivative, i.e., change in fiber density dynamics (Fig. 3B-C). The correlations in fiber density is attributed to the monotonic increase in ECM densification near single and pairs of communicating cells (Fig. 2B and Fig. 2D). The correlations in the temporal derivative of fiber density is attributed to the association between fiber density and the change in

fiber density (Fig. 2E-F): ECM became denser over time, leading to increased temporal derivatives. However, these general trends lead to high correlations between any two cells regardless whether they communicate with each other, and confound the unique fluctuations that may be attributed to a specific pair of communicating cells. Thus, we aimed at dampening the outer correlations so non-communicating outer regions will have no notable correlations, while maintaining some correlation between the communicating inner regions. This was achieved by detrending, i.e., removing the temporal trends via a second temporal derivative (Fig. 3B-C, Fig. S5A-F, Methods). The second temporal derivative also showed consistent results of no correlation between two (non-communicating) single cells (Fig. S5G). Although the outer correlations were lost with a second temporal derivative, the inner correlations were also lost and we were unable to distinguish between the simulated- inner and outer correlations. This was apparent by plotting the matched inner-outer correlations in 2D, that were distributed around the "Y (outer) = X (inner)" line (Fig. 3D-E, $\sigma = 0$).

We suspected that the inability to distinguish the simulated- inner from the outer correlations was due to lack of variability in ECM remodeling over time. Every simulated cell contracted in the exact same magnitude as any other simulated cell, leading to a nearly exact time-dependent remodeling of the adjacent ECM regime, thus masking the effect of the propagating communication signal on the correlation. Thus, our hypothesis was that variability in the cells' contraction activity will lead to variability in the local ECM remodeling, that will enable us to decouple the ECM remodeling that occurs near any cell to the specific signal that is transmitted from a specific communicating partner. This will define a unique fingerprint that could be used to quantitatively characterize the inner correlation of a pair of communicating cells. Indeed, when introducing heterogeneity in cell contraction, we distinguished inner from outer correlations while maintaining the non-communicating outer correlations around zero (Fig. 3D-E, Video S6). Cell heterogeneity was included in the simulations by drawing the instantaneous contraction rate of each cell independently from a normal distribution with mean (μ) contraction of 1% and a standard deviation (σ) in the range of 0-0.75% (std.) (Methods). Even a minimal standard deviation of 0.25% in cell contraction was sufficient to make a clear distinction between inner and outer correlations, i.e., the inner correlation was greater than the outer correlation for cell pairs, which improved with increasing standard deviations (Fig. 3D-E). This inner-outer discrimination by cell heterogeneity was negatively correlated to the pair distance - as cells were

placed further apart, it became more difficult to distinguish inner from outer correlations (Fig. S6, Video S7). Moreover, the inner-outer discrimination was improved when moving the ECM quantification window along the band, toward the communication partner, which increased the communication partner's influence, and led to increased inner correlation (Fig. S7, Video S8). Altogether, these results established the notion that temporal correlation of local ECM remodeling dynamics can distinguish between inner regions, located in-between simulated pairs of communicating cells, from outer regions and that contractile heterogeneity is required to quantitatively identify cell-ECM-cell communication.
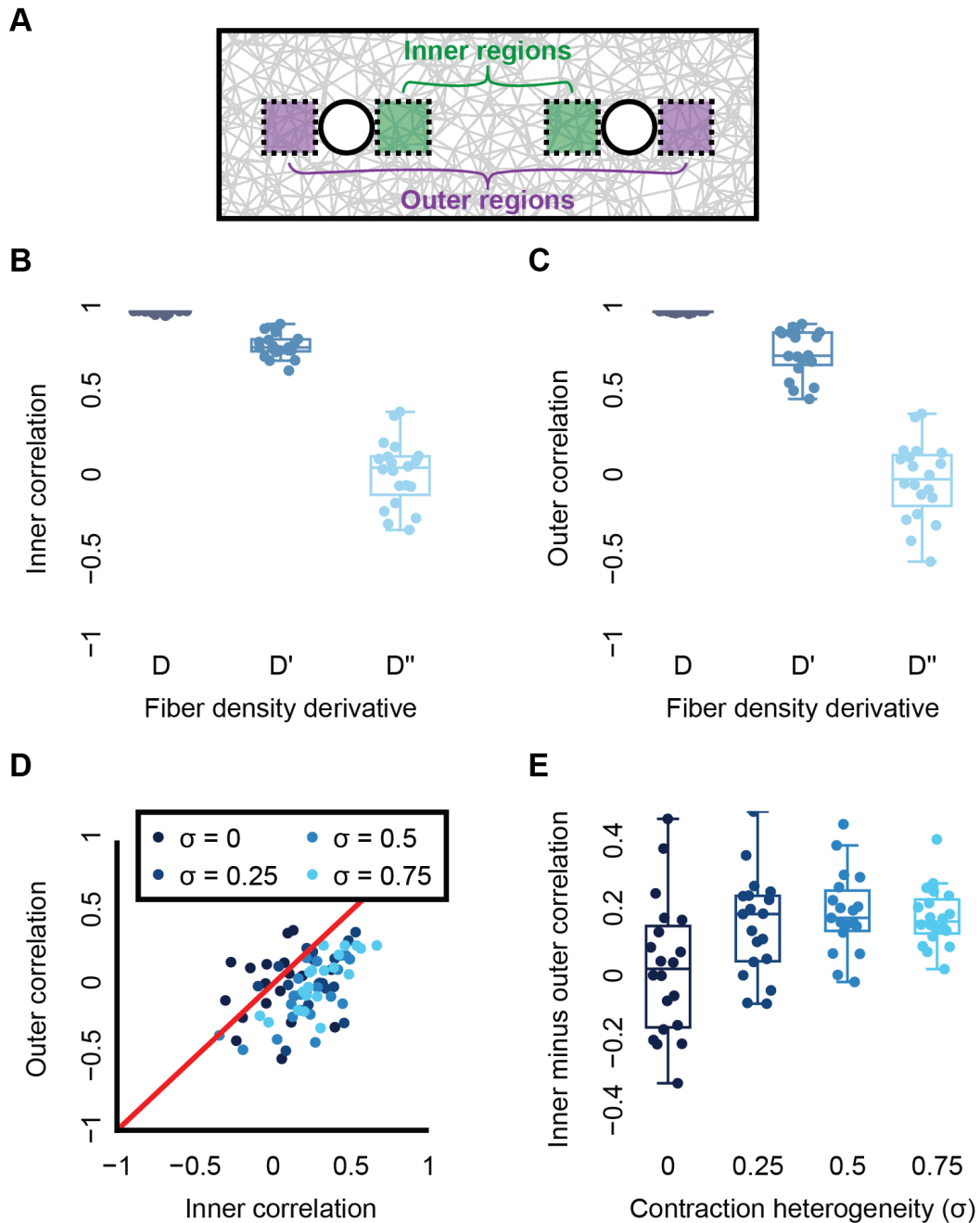
Figure 3: Using temporal correlations of fiber remodeling dynamics to distinguish regions located along the band (inner correlation) of communicating cells from non-communicating regions (outer correlations) in simulations. (**A**) Schematic sketch. Inner regions (green) adjacent to the cells along the axis between them. Outer regions (purple) adjacent to the cells along the axis defined between them. (**B-C**) Inner and outer correlations for fiber density (D), first temporal derivative (D') and second temporal derivative (D''). N = 20 cell pairs at a pair distance of 5 cell diameters. (**B**) Inner correlations. Wilcoxon signed-rank testing the null hypothesis that the correlations are distributed around a mean = 0: p-value < 0.0001 (D), < 0.0001 (D') and not significant (D''). (**C**) Outer correlations. Wilcoxon signed-rank testing the null hypothesis that the correlations are distributed around a mean = 0: p-value < 0.0001 (D), < 0.0001 (D') and not significant (D''). (**D-E**) Heterogeneity in cell contraction enables the distinction between matched

inner and outer correlations. Pair distance of 5 cell diameters. Correlations were calculated from the second derivative of fiber density dynamics. Color code (σ) indicates the standard deviation of the normal distribution (with mean = 1% contraction) that single cells draw their contraction from at each time frame. Wilcoxon signed-rank testing the null hypothesis that the differences of inner minus outer correlations are distributed around a mean = 0: σ = 0, not significant (N = 20 pairs); σ = 0.25, p-value < 0.001 (N = 19 pairs); σ = 0.5, p-value < 0.001 (N = 19 pairs); and σ = 0.75, p-value < 0.0001 (N = 20 pairs). (**D**) Inner versus outer correlations. Red y = x line reflects the situation where the inner correlation is equal to the outer correlation (see also S6). (**E**) The distribution of the deviations of inner from their corresponding outer correlations (subtraction of outer from inner correlations) for each level of heterogeneity.

Distinguishing between pairs of communicating cells using temporal correlation of local ECM remodeling dynamics

Definitive quantification of cell-ECM-cell communication lies in the ability to distinguish between pairs of communicating cells, i.e., whether the cell-ECM-cell communication of one pair of cells can be distinguished from a different pair of communicating cells. We tackled this challenge by testing whether the inner correlation between a simulated pair of communicating cells surpassed the correlation between one cell from that pair and another cell from a different simulated pair of communicating cells in a different fibrous network (Fig. 4A). Specifically, we compared the correlation in the second temporal derivative of the local ECM density dynamics between quantification windows adjacent to each cell pair, located in the 'same' pair versus a cell in a 'different' pair, and accordingly coined the term *same-versus-different pair analysis* (schematic in Fig. 4A). Having the "same" correlation exceed the "different" correlation implies that the correlation between a communicating cell pair is not merely an effect of a similar ECM densification pattern that is common to any pair of communication cells, but rather is indicative of communication unique for the "same" cell pair at test. We considered all possible ordered combinations of triplets of cells that include a pair of communicating cells and a third cell that takes part in a different communicating cell pair. "Same" pair had a higher correlation than a "different" pair in 92% of the matched correlations for pair distance of 4 cell-diameters, and this correlation gradually reduced with increased pair distance (Fig. 4B-C). Thus, simulated cells communicating with one-another were more synchronized in their ECM remodeling dynamics, and same-versus-different analysis could distinguish between different pairs of communicating cells.

12

Non-genetic phenotypic cell contractile heterogeneity, which we artificially introduced to simulations, and was necessary to identify cell-ECM-cell communication, is an inherent cellular property (e.g., [31]). Thus, we aimed at extending our simulation results of distinguishing between pairs of communicating cells to experimental data. The first temporal derivative was sufficient to remove non-stationarity effects in ECM remodeling dynamics of single and pairs of communicating fibroblast cells (Fig. S8), so we could avoid the second derivative in the correlation analysis of experimental data. We performed the same-versus-different pair analysis, but were able to quantitatively distinguish between different pairs of communicating fibroblast cells only after shifting the quantification window slightly above or below the axis connecting the communicating cells (Fig. 4D-E, Fig. S9). "Same" pair had a higher correlation than "different" pair in 97% of the matched correlations (Fig. 4D). This demonstration of distinguishing pairs of communicating cells was consistent for various pair distances (Fig. 4E, Fig. S10) and even for different cell pairs within triplets of cells (Fig. 4F-H). Experiments imaged at faster temporal resolution (5 minutes per frame, Methods) determined that faster imaging enhances the capacity to distinguish pairs of communicating cells (Fig. S11, Fig. S12).

Importantly, since all cells in a single experiment were embedded in the same network, ECM deformations might correlate in nearby regions without necessarily involving cell-ECM-cell communication. Thus, we had to control for spurious correlations that could originate from the proximity between the ECM regions in the same network. Careful analysis that considered ECM regions (without cells) located close to each other verified that we are indeed able to identify cell-ECM-cell communication that had higher inner correlations compared to their matched non-cellular "fake" cell pairs (Fig. S13, Fig. S14, Methods).

A

Same network

Different network

B 72% "same" > "different"

Different network correlation

Same network correlation

C 92% 79% 70% 68%

Same minus different correlation

Pair distance (cell diameter)

D 97% "same" > "different"

Different network correlation

Same network correlation

E 96% 95% 92%

Same minus different correlation

Pair distance (cell diameter)

F

G

Cells 1 & 2
Cells 1 & 3
Cells 2 & 3

Different network correlation

Same network correlation

H

Triplet #1
Triplet #2
Triplet #3

Different network correlation

Same network correlation

14

Figure 4: Distinction between pairs of communicating cells. (**A**) Schematic sketch of the *same-versus-different pair analysis*. The correlation between quantification windows of communicating pairs ("same", green) is evaluated in relation to the correlation between one cell from that pair and another cell from a different communicating pair ("different", purple). (**B-C**) Same-versus-different pair analysis in simulations. Each data point shows the correlation between the "same" and "different" cell pairs using the second derivative of fiber density dynamics. Mean contraction of 1% and standard deviation of 0.5%. All combinations of "same"/"different" were considered. (**B**) Pair distances: 5 (N = 19), 7 (N = 19) and 9 (N = 19) cell diameters. "Same" pair had a higher correlation than "different" pair in 72% of the matched correlations. (**C**) "Same" - "different" correlation distributions for different pair distances: 4 (N = 20 pairs), 5 (N = 19 pairs), 7 (N = 19 pairs), and 9 (N = 19 pairs) cell diameters. 92% (pair distance = 4), 79% (pair distance = 5), 70% (pair distance = 7) and 68% (pair distance = 9) of data points were positive, implying that the "same" correlation is higher than the "different" correlation. Wilcoxon signed-rank testing the null hypothesis that the data are distributed around a mean 0: p-value < 0.0001 for all pair distances. (**D-E**) Same-versus-different pair analysis in experiments. Quantification windows were placed ~0.5 cell diameter (7.5 µm) above the connecting axis between the cells (see Fig. 5E for schematics). Correlations were calculated using the first derivative of fiber density dynamics. (**D**) Pair distance = 60-150 µm (~4-10 cell diameters). N = 25 cell pairs, all combinations of "same"/"different" were considered. "Same" pair had a higher correlation than "different" pair in 97% of the matched correlations. (**E**) "Same" - "different" correlation distributions for different pair distances: 4-6 (N = 9 pairs), 6-8 (N = 12 pairs), and 8-10 (N = 4 pairs) cell diameters. "Same" pair had a higher correlation than "different" pair in 96% (pair distance 4-6), 95% (pair distance 6-8) and 92% (pair distance 8-10). Wilcoxon signed-rank test p-value < 0.0001 for all pair distances. (**F**) Triplet of cells (left) communicating with one another (right) after 255 minutes of live cell imaging. Scale bars = 15 µm. (**G-H**) Same-versus-different pair analysis for cell triplets. Quantification windows were placed ~0.5 cell diameter (7.5 µm) above the connecting axis between the cells. Correlations were calculated using the first derivative of fiber density dynamics. (**G**) Same-versus-different pair analysis for the cell triplets from panel F. Pair distances 7.3 (Cells 1 vs. 2), 6.3 (Cells 1 vs. 3) and 4.9 (Cells 2 vs. 3) cell diameters. "Same" pair had a higher correlation than the "different" pair in 7/8 (Cells 1 & 2), 8/8 (Cells 1 & 3) and 8/8 (Cells 2 & 3) of the matched correlations. Wilcoxon signed-rank test p-value < 0.05. (**H**) Multiple triplets. N = 3 triplets. Triplet #3 was presented in panels F-G (matched orange color). 97% of matched same minus different correlations were positive. Wilcoxon signed-rank p-value < 0.0001.

Decoupling band formation and communication sensing

Our finding that cell-ECM-cell communication can be identified quantitatively only when shifting the quantification window away from the connecting axis between the cell centers, encouraged us to systematically measure the relations between cell-ECM-cell communication and band formation in experiments. We analyzed different ECM quantification windows in the 3D space around the cell by shifting them laterally (perpendicular, in the XY axis) and axially (up and down, in the Z axis) in relation to the connecting axis (Fig. S15, Methods). For each shifted window we measured the final normalized fiber density after 255 minutes and also, independently, performed same-versus-different pair analysis for the corresponding windows over time. While the fiber density was maximal along the connecting axis, we were surprised to

discover that the discrimination between different pairs of communicating cells was optimized above or below (axially) the connecting axis (Fig. 5B-C), and excluded the possibility that this was an artifact of saturated pixels along the dense fibrous band (Fig. S16). These results were consistent for faster imaging experiments (Fig. S17) establishing that communication sensing, i.e., our method's ability to identify cell-ECM-cell communication, is decoupled from band formation.

This decoupling between band formation and communication sensing led us to ask whether we can identify cell-ECM-cell communication for cell pairs that did not form a visible band of denser fibers between the cells. Indeed, same-versus-different pair analysis identified cell-ECM-cell communication for band-less pairs, slightly above or below the connecting axis, implying that communication is present even when a band is not visible to the human eye (Fig. 5E-I, Fig. S18, Video S9).

We conclude that our method's ability to measure communication is improved when correlating quantification windows located slightly away from the connecting axis in-between the communicating cells, while the densest fiber band is formed directly along the connecting axis. These results challenge the current notion that band formation is the hallmark of cell-cell communication in fibrous gels.

A

Connecting axis
Z axis
XY axis

B Fiber density

Offset in Z axis (cell diameter)

Z-score

Offset in XY axis (cell diameter)

C "Same" > "different"

Offset in Z axis (cell diameter)

Fraction

Offset in XY axis (cell diameter)

D

Fiber density
Communication

Fiber density (z-score)

"same" > "different" (%)

Offset in Z axis (cell diameter)

E

Connecting axis
Z axis
XY axis

F

Begin

End

G

Left
Right
Middle

Fiber density (z-score)

Time (minutes)

H 70% "same" > "different"

Different network correlation

Same network correlation

I

97%   70%

Same minus different correlation

Band   No Band

Figure 5: Spatial decoupling of band formation and cell-ECM-cell communication. (**A**) Cell pair axes schematic sketches. Z-axis (cyan) and XY-axis (purple) are perpendicular to each other and to the connecting axis between the cells' centers (black). (**B-D**) Mean fiber density and cell-ECM-cell communication for shifted quantification windows in cell pairs with a visible band. Pair distances of 60-150 μm (~4-10, cell diameters). The dashed vertical line in panels B-C is used as a line profile in panel D. (**B**) Fiber density. Mean fiber density for systematic offsets in Z and XY axes. (**C**) Cell-ECM-cell communication. Mean fraction of higher "same", correlation between communicating pairs, versus "different", correlation between one cell from that pair and another cell from a different communicating pair for systematic offsets in Z and XY axes. Red 'x' marked that the null hypothesis that "same" - "different" correlations are distributed around zero was not rejected with p-value ≤ 0.05. (**D**) Fiber density and cell-ECM-cell communication along the axial linescan (offset in XY axis = 0). Peaks in cell-ECM-cell communication appear above (and below) the connecting axis between the cells, where fiber density is maximal. (**E**) Optimal quantification window location to quantify cell-ECM-cell communication. Offset in Z axis = 0.5. Offset in XY axis = 0. Top: schematic sketch. Bottom: Representative pair of communication cells after 255 minutes of imaging. Scale bar = 15 μm. Line connects the cell centers in the XY/Z space. For the displayed pair the Pearson correlation coefficient was 0.66 (Z offset = 0) and 0.71 (Z offset = 0.5). (**F-I**) Cell-ECM-cell communication for cell pairs with no visible band. Quantification windows were placed 7.5 μm (~0.5 cell diameter) above the connecting axis between the cells. (**F**) Representative cell pair with no visible band at the onset ("begin") and after ("end") 255 minutes of cell imaging. Scale bar = 15 μm. (**G**) Quantification of the dynamics of the first derivative of fiber density in the cell pair in panel F. Left/right - quantification windows adjacent to cell boundaries, "middle" - quantification window in between the cells centers at each time frame. Pearson correlation coefficient between left and right cells inner regions = 0.7, p-value < 0.0001. (**H**) Same-versus-different pair analysis for cell pairs with no visible band. Pair distance = 60-150 μm (4-10 cell diameters). N = 14 cell pairs. Each data point shows the correlation between the "same" and "different" cell pairs using the second derivative of fiber density dynamics. All combinations of "same"/"different" were considered. "Same" pair had a higher correlation than "different" pair in 70% of the matched correlations. (**I**) "Same" - "different" correlation distributions for pairs with and without a visible band. 97% (With band) and 70% (Without band) were positive, implying that the "same" correlation is higher than the "different" correlation. Wilcoxon signed-rank test for the null hypothesis that the data are distributed around a mean of 0 was rejected with p-value < 0.0001 for both scenarios.

Matchmaking: quantitative identification of communication partners

Given our ability to distinguish one pair from a different pair of communicating cells, we wondered whether we can match a cell to its true communication partner when considering all other cells in the experiment (Fig. 6A, Video S10, Methods). For each cell, in every cell pair with a visible band, we recorded the first derivative of its fiber density dynamics, correlated it to all other cells in the experiment, and reported the rank of its true matching partner. With 49 potential partners, the expected random probability of identifying the communication partner is 1/49 ~ 0.02 (Fig. 6B). However, using the correlation-based matching in quantification windows located 7.5 μm above the connecting axis between the cells, the probability of identifying the true communication partner was 0.68 (Fig. 6C). This accuracy of identifying the matching

partner dropped to 0.12 when considering quantification regions along the connecting axis between the cells (Fig. 6D) and was not attributed to the proximity between the ECM regions in the same network ("fake" pairs, Fig. 6E). Faster imaging at 5 minute resolution led to perfect matching between communicating cell pairs (Fig. 6F, N = 28 potential partners of each cell, expected random probability of 0.09), and even for a 0.95 accuracy in matching communicating pairs without a visible band (Fig. 6G, N = 112, expected random probability of 0.02). These successes in matching communication partners highlights the high sensitivity of our approach.
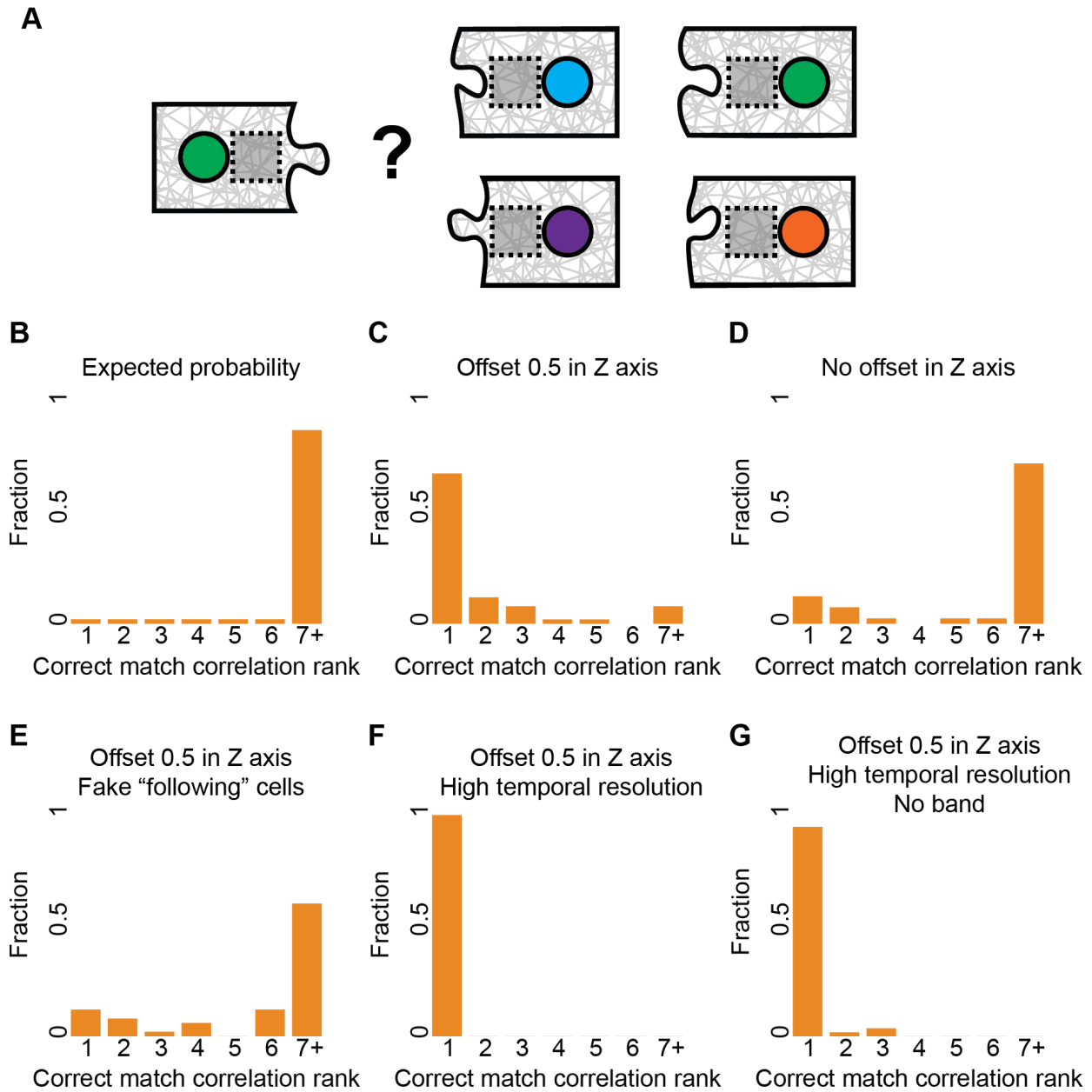
Figure 6: Matchmaking between communication partners. (**A**) Schematic sketch. ECM remodeling dynamics of a given cell (left) is correlated with the rest of the cells in an experiment (right). The rank of the correlation with the true communication partner (i.e., the position in the sorted list of all correlations with other cells, marked in green) is recorded. This process repeats for all cells. (**B-E**) Distributions of the correlation rank with the true communication partner for cell pairs with a visible band. Pair distance of 60-150 μm (~4-10 cell diameters). Correlations were calculated using the first derivative of the fiber density dynamics. "Correct match" refers to a correlation rank of 1. (**B**) Random matching: simulation of arbitrary matching leads to correct matching probability of 0.02 (N = 50 cells). (**C**) Quantification window 0.5 cell diameters (7.5 μm) above the connecting axis between the cells: correct matching probability of 0.68 (N = 50 cells), compared to 0.02 for random matching (panel B). (**D**) Quantification window at the connecting axis between the cells: correct matching probability of 0.12 (N = 40 cells), compared to 0.02 for random matching. (**E**) ECM regions (without cells) located close to each other

("fake-following" pairs, see Fig. S13A for schematics): correct matching probability of 0.12 (N = 50 cells), compared to 0.02 for random matching. (**F**) Higher temporal resolution (5 minutes per frame) and quantification window 7.5 μm above the connecting axis between the cells: perfect matching (probability = 1, N = 28 cells), compared to 0.09 for random matching. (**G**) Higher temporal resolution (5 minutes per frame), cell pairs without a visible band, and quantification window 7.5 μm above the connecting axis between the cells: correct matching probability of 0.95 (N = 112 cells), compared to 0.02 for random matching.

Identifying leader and follower in pairs of communicating cells

We next asked if we could use our approach to quantify asymmetric interactions between the communicating partners. More specifically, can we identify which cell in a communicating pair is more dominant or influential? Our quantitative interpretation of "influential" is that past ECM-remodeling fluctuations of one cell are predictive of the future ECM-remodeling of its communicating partner. Such temporal order defines a leader-follower relation. We performed simulations where a "follower" cell "imitates" the previous contraction of its influential "leader cell". In other words, the contraction of both cells are determined by the leader cell with a time lag of one round (Fig. 7A). The simplest approach to quantitatively identify a temporal order is by cross correlation with time lags, where the correlation between two time-series is calculated for a given lag, and the time-lag that leads to the maximal correlation determines the temporal order. This analysis successfully identified which cell was the leader and which one was the follower with an accurate lag time (Fig. 7B, Fig. S19A). To evaluate the robustness of using correlations to identify leader-follower relations we simulated cell pairs where the follower contraction was composed of an independent component, and a component that is dependent on its leader: $Contraction_{follower}(t) = (1 - \alpha) * N(\mu, \sigma) + \alpha * Contraction_{leader}(t - 1)$, where $t > 1$, $0 \le \alpha \le 1$, $\mu = 1$, $\sigma = 0.5$ are the mean and standard deviation correspondingly, and $Contraction_{leader}$ is drawn from the normal distribution $N(\mu, \sigma)$. The term α indicates the "followership" magnitude, higher values of α imply that the follower is more influenced by its leader contraction. The inner correlation increased with increased influence of the leader cells (Fig. 7C) and the maximal cross correlation occurred at the correct lag, accurately identifying the leader/follower roles for all simulated pairs for $\alpha = 0.5$, where the follower cell contraction is determined with equal contribution from its intrinsic "decision" and the extrinsic influence by its leader (Fig. 7D, Fig. S19B). In a second validation we tested whether we can identify leader/follower when the follower contracts more than its leader. This leads to increased ECM

remodeling that might propagate to the leader cell and mask its influence on the follower. We set α to 1 (follower is copycatting the leader's contraction), and introduced $\beta \geq 1$ - the fold increase of the follower's contraction: $Contraction_{follower}(t) = \beta * Contraction_{leader}(t-1)$. The inner correlation was nearly identical for $\beta \leq 1.2$ (20% increase in follower contraction), and the first mistaken prediction of the follower/follower assignment occurred for $\beta = 1.2$, for 1 out of 7 simulated pairs (Fig. 7E, Fig. S19C). We further validated these results by pairing leaders or followers to cells from other communicating pairs to create artificial pairs of cells that did not interact with one another (Fig. S20). These results verified that we can robustly identify leader and follower cells in simulated communicating cells from their ECM remodeling fluctuations.

Cross correlation analysis did not identify leader-follower relations in experimental data (Fig. S21) and thus we turned to a more powerful statistical technique, termed Granger Causality (GC), to infer cause-effect relationships from fluctuating time-series data[32]. GC is an asymmetric measure for the extent of which the prediction of values in one time series can improve by including information from another time series. Briefly, this is achieved by calculating a linear regression model to predict the future of time series A from its own past, and then applying a statistical test against the null hypothesis that including additional information from the past values of another time series B does not improve prediction accuracy (full details in the Methods). Rejection of this null hypothesis suggests that B is influencing A. Granger Causality analysis identified 5 out of the 21 imaged cell pairs to include a leader and/or follower cell (Fig. 7F, Fig. S22, Video S11, Video S12). These results suggest that Granger Causality has the potential to identify how one cell is indirectly influenced by a propagating mechanical signal from the communication "leader" partner (as depicted in Fig. 1A).
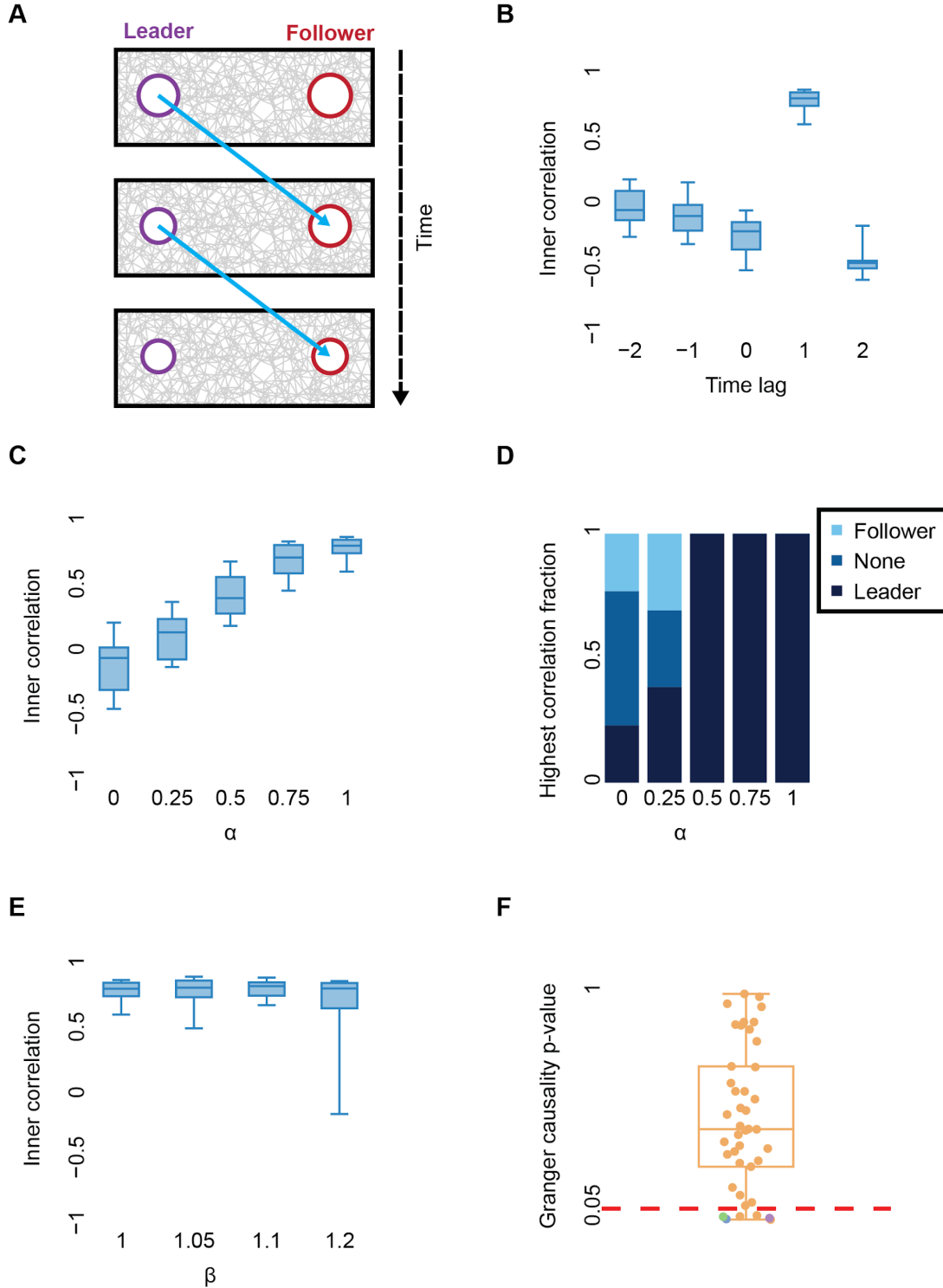
Figure 7: Identifying leader-follower relation in communicating cell pairs. (**A**) Schematic sketch of the simulation. Right cell (red, follower) mimics the contraction of the left cell (purple, leader) at the previous time point (Methods). (**B-E**) Simulated inner cross correlation for different time lags. N = 13 cell pairs. Pair distance = 7 cell diameters. The leader cell draws its contraction in each step independently from a normal distribution with mean of 1% and standard deviation of 0.5%. The follower cell draws its "intrinsic" component (contraction_follower) from the same distribution. The second derivative of the fiber

23

density dynamics was used for correlation. Time lag is applied to the follower's time series before correlation is calculated. (**B**) Distribution of inner correlations as a function of the time lag. (**C-D**) Identifying leaders and followers as a function of varying values of α. Increased α values imply an increased contribution of the extrinsic component - the influence by the leader cell. (**C**) Distribution of inner correlation with time lag = 1 as a function of α values. (**D**) Fraction of cell pairs where the leader (time lag 1 or 2), follower (time lag -2 or -1) or none (time lag 0) lead to maximal inner correlation, and is thus identified as leader, as a function of α values. (**E**) Distribution of inner correlation with time lag = 1 as a function of β values. Increased β implies an increased contraction by the follower cell. α value was set to 1. (**F**) Experimental analysis with Granger Causality (GC). N = 21/73 cell pairs (42 asymmetric statistical tests) passed the whiteness test of no autocorrelation in the residuals (Fig. S23). Temporal resolution = 5 minutes per frame. Pair distance 60-150 μm (4-10 cell diameters). Quantification windows placed 7.5 μm, above the connecting axis between the cells (see Fig. 5E for schematics). Granger causality analysis was applied using the first derivative of fiber density dynamics. Each data point is the GC p-value. The null hypothesis is rejected with p-value < 0.05 without multiple hypothesis correction (p-value < 0.15 with FDR correction[33]) for 6/42 of the GC tests (5/21 of the cell pairs): where one out of two cell pairs had a visible band, four pairs (one with, three without a visible band) had leader-follower assignment and one pair with bidirectional GC (without a band). Green datum presented in Fig. S22A-C. Blue datum and purple (left cell causing) presented in Fig. S22D-F.

Discussion

We proposed here a systematic computational method to quantify cell-ECM-cell interactions and demonstrated its applicability in simulations and experiments. Our method quantifies the local fiber remodeling dynamics between pairs of communicating cells in 2D (simulations) and 3D (experiments) by applying the following key steps. Normalization in relation to the background to enable robust comparison across experiments and between simulations and experiments; Detrending to avoid spurious correlations; Systematic evaluation of the location of the quantification window to extract the most informative signal; Measurement the temporal correlation; and application of cross-correlation or Granger Causality analysis.

We combined finite element simulations and live cell imaging experiments. Our simulations served two purposes; On the one hand, raising specific biophysical hypotheses that could then be verified experimentally, and on the other hand, as a viable tool to control various independent parameters in order to test and verify the sensitivity of our approach. An example of raising specific biophysical hypotheses includes the discrepancy between simulations and experiments in the magnitude of fiber density between cell pairs (Fig. 1G). This serves as evidence that a cell is actively responding to ECM fluctuations induced by its communication partner. Another example is the positive feedback between fiber density and its magnitude of remodeling that was revealed in simulations before being validated experimentally (Fig. 2E-F). Examples of assessing the sensitivity and the robustness of our approach include examining the minimal cell contractile heterogeneity required to effectively quantify cell-ECM-cell communication (Fig. 3, Fig. 4B-C), and testing our sensitivity to cell autonomously and contraction magnitude that may mask the capability to identify leader-follower relations (Fig. 7B-E).

We applied our method to follow the universal stages of long-range cell-cell mechanical communication: when a cell deforms the ECM, the mechanical signal propagates throughout the network reaching other cells, that change their internal state in response (Fig. 1A). The mechanical signal is expected to propagate through the microenvironment in less than a second[34], while changes in the cell's molecular organization, and cell action, occurs in minutes-to-hours, fitting the time scales of the band formation process. We discovered that the fiber density at the intercellular bands was amplified by a positive feedback between the fiber density and the change in fiber density contributing to effective band formation in pairs of communicating cells

(Fig. 2E-F). However, the denser bands formed in experiments compared to simulations (Fig. 1G) could not be explained by this positive feedback, which was more dominantly observed in simulations (Fig. 2: E versus F). We suggest that the discrepancy between simulations and experiments in fiber densification in cell pairs compared to single cells may be explained by cells actively altering their internal state in response to the mechanical signal they sense from the other cell through the microenvironment, a cellular property that was not simulated. Indeed, cells were previously shown to respond to local aligned and stiffened ECM by applying more forces[35]. Unlike our simulations, where cell shape is circular and contraction is uniform around the cell, in experiments, cells can adjust their shape to become more anisotropic (polarized), and extend protrusions toward their communication partner. This can lead to higher concentration of forces in the direction of the neighboring cell, resulting in the observed increase in ECM density. Leader-follower analysis (Fig. 7) provides another supporting evidence that cells actively respond to the mechanical signal transmitted by their communication partner. Our ability to measure how a cell is actively responding to the mechanical signals transmitted from the communicating partner opens new venues for future research to decipher how cells process mechanical information transmitted through the microenvironment.

We found that heterogeneity in cell contractility created unique temporal patterns of ECM fluctuations that were necessary to quantitatively identify cell-ECM-cell communication, allowing us to distinguish between different pairs of communicating cells using temporal correlation of local ECM remodeling fluctuations. Cell-ECM-cell communication occurred even when a band between the cells was not visible and our ability to measure communication was optimal in a quantification window located about 0.5-1.5 cell diameters above or below the connecting axis between the cells. We propose that the impairment of measuring cell-ECM-cell communication along the band stems from alterations of the mechanical properties of the fibrous network in the band[7,9]. We recently reported that ~80% of the band volume deformation is permanent - not returning to its undeformed state after blocking cell forces[15]. This plastic deformation along the dense fibrous band between the cells, may restrict the mechanical signal that propagates between the cells, or our ability to measure it via ECM fluctuations, in both cases, leading to reduced correlations and impairment in identifying cell-ECM-cell communication in relation to the off-band regions that remain less dense and maintain their

elastic properties. Some support to this hypothesis is presented in Fig. S24, demonstrating a drop in cell-ECM-cell communication in denser band regions.

We also aimed at identifying leader-follower relationships. We simulated a situation where one cell influenced its communicating partner, determining its future contractions and demonstrated that our method can robustly identify the leader and follower cells from the ECM-remodeling fluctuations. This was even possible in challenging scenarios where followers were only partially influenced by their leader or contracted more than their leader (Fig. 7C-E). We also identified leader-follower relations in a small subset of the live imaged cell pairs (Fig. 7F), providing a proof-of-concept demonstration, that should be extended in future studies, to formally establish the notion of communication properties and relations between cells in long-range mechanical cell-cell communication. This will be achieved by faster imaging of more cells in different molecular/functional states or from different genetic backgrounds.

We used standard confocal imaging in this study, which is inherently limited in its temporal resolution, axial resolution and size of field of view. Despite these limitations, we succeeded to quantitatively characterize intercellular mechanical communication through fibrous environments, being able to perfectly match all communication partners, with 28 candidates for each match, only from ECM remodeling fluctuations (Fig. 6F). This performance, especially given the standard microscopy that is available in almost any academic institute, highlights the potential of democratizing cell-ECM-cell communication quantification.

Our proof of principle study is an enabler of mechanistic understanding of long-range cell-cell mechanical communication, and sets the ground for potential applications. Having the ability to quantitatively measure cell-ECM-cell communication, could enable to systematically probe the cellular and molecular players for this mode of mechanical communication, naturally starting with the actomyosin cytoskeleton and adhesion complexes[18]. We expect that our method could be generalized to non-fibrous environments, such as synthetic (e.g., poly-acrylamide hydrogels) or biological (e.g., Matrigel) hydrogels, by embedding tracer particles that will enable the indirect measurement of local ECM remodeling fluctuations. Another exciting venue is deciphering the role of long-range intercellular communication in the more complex and physiological relevant microenvironments in vivo. A third extension of our method would be to apply it to other modes of cell-cell communication. For example, using intracellular molecular

27

fluctuations as the functional readout to infer cell-cell communication, an approach previously taken in[36] to reveal signaling ordering at the intracellular scale.

One application where the ability to precisely measure cell-cell communication may be useful is tissue engineering. By controlling the patterning of multiple cell types one could optimize tissue formation according to cell type specific communication capabilities[37]. Another application is high content 3D image-based screening. Image-based phenotypic screening is traditionally applied with 2D imaging, quantifying single cell morphology and distributions of intracellular fluorescent intensities, and is applied for multiple application including identification and characterisation of small molecules in drug discovery[38]. Recent tools enable high-content 3D image-based cell phenotyping[39], providing a more physiologically relevant context for in vivo followup studies[40]. The interplay between 3D cell morphology, the interactions with the environment and the mechanical communication with other cells could provide important complementary functional readouts for 3D image-based phenotypic cell phenotyping that are not accessible with current methods. Such phenotyping could be very useful for applications where the cellular microenvironment and the interactions between cells and the ECM are established hallmarks, such as in cancer or fibrosis screening[23,25,41,42].

Methods

Computational Modeling

Finite element simulations of cells contraction in fibrous networks

We used our previously described computational finite element model of one or two cells contracting in two-dimensional fibrous networks[11,43,44]. We used the finite element software Abaqus/CAE 2017 (Dassault Systèmes Simulia) to model the network mechanics and perform the simulations. The software's Standard\Implicit solver was used in all simulations. The cells were modeled as circular voids in the fiber networks. The fibers were represented by discrete one-dimensional elements connected by nodes (Fig. S25A), randomly distributed to set an isotropic and homogeneous network structure prior to cell contraction (see next). The output of each finite-element simulation included the information regarding each network element's location and dynamics.

Fiber network architecture

We used Matlab R2018b to construct the network geometry and architecture as previously described[11]. The networks were designed to optimize the fiber orientations distribution toward uniformity (i.e., isotropic) and toward homogeneous fiber density. Briefly, we devised a random process to create network geometries, as we previously reported in [11]. The process starts from uniformly scattering nodes in a circular domain. The nodes were then connected by fiber elements by considering an objective cost function which controls the fiber length, fiber connectivity (i.e., the mean number of fibers intersected at each node) and the angle between fibers connected at each node. The network coordinates spanned from -2 to 2 (AU) in X- and Y-axis (Fig. S25B). Cell centers were located along the X axis, with a cell diameter of 0.08 (Fig. S25B). The mean fiber thickness was 0.2 AU, and mean fiber length was 20 AU, fitting typical fiber density-to-length ratio for collagen\fibrin gels[44–46]. The cell diameter before contraction was set to 0.08 AU, so that the cell diameter/mean fiber length ratio was 4:1, a typical ratio for fibroblast cells embedded in fibrin gel[44]. The average connectivity of the network was set to eight, to balance the tradeoff between the finite element software numerical stability and physiological relevance.

The mechanical properties of the simulated fiber networks

Fibers were connected to one another by nodes, which acted as a freely rotating hinge, allowing for a rotation of the fibers without resistance. The fibers were modeled as linear truss elements, undergoing uniaxial tension or compression, without bending. They were characterized by nonlinear behavior typical to ECM fibers, including buckling under compression[10,12] and stiffening under tension[13,47]. We represented the buckling of the fibers by an elastic modulus which was ten times smaller at compressive strains exceeding 2% relative to the elastic modulus at small strains (-2% to 2%). Stiffening was achieved by an exponential increase in the elastic modulus for tensile strains larger than 2% [11,44,48]. In all simulations, the outer boundary of the network was fixed for translations and rotations.

Simulating cell-ECM-cell communication

Cell contraction was modeled by applying a boundary condition of radial isotropic contractile displacements to all nodes constituting the cell boundaries, reaching up to 50% contraction of the cell radius. To simulate time we consecutively applied 1% cell contraction for 50 steps, reaching a final 50% cell contraction. Heterogeneity in cell contraction was implemented by applying cell contraction selected from a normal distribution with a mean (μ) of 1% and varying standard deviations (σ) of 0, 0.25, 0.5 or 0.75, in each simulation step. In all simulations, the network size was set to 50 cell diameters and the cells were placed in its center to prevent boundary effects.

Leader-follower simulations

These simulations were implemented such that one cell (the "follower") contracted with a dependency on the other cell (the "leader"). The leader contraction at each time point was selected from a normal distribution $N(\mu = 1\%, \sigma = 0.5\%)$. In the first time step, the follower contraction was drawn independently, from the same normal distribution. From the second step and onwards, the follower contraction was composed of two components:

$$Contraction_{follower}(t) = (1 - \alpha) * N(\mu, \sigma) + \alpha * Contraction_{leader}(t - 1)$$

where $Contraction_{follower}(t)$ is the follower intrinsic contraction at time step t drawn from $N(\mu = 1\%, \sigma = 0.5\%)$ and $Contraction_{leader}(t - 1)$ is the leader's contraction at the previous time step drawn from the same distribution. α is a constant that varies between 0 and 1 and defines the level of leader-follower dependency: $\alpha = 0$ is the case of independently contracting cells and $\alpha = 1$ is the case where the follower cell repeats the leader's contraction with 1 frame

delay (see Fig. 7A). In the second leader-follower simulation, the follower contracts according to the following equation: $Contraction_{follower}(t) = \beta * Contraction_{leader}(t-1)$

where $\beta > 1$, thus imitating the leader with a certain augmentation.

Experiments

Cell culture

Swiss 3T3 fibroblasts stably expressed GFP-actin (obtained as gifts from S. Fraser, University of Southern California, Los Angeles, CA) were cultured in DMEM supplemented with 10% fetal bovine serum, nonessential amino acids, sodium pyruvate, L-glutamine, 100 units/ml penicillin, 100 µg/ml streptomycin, and 100 µg/ml Neomycin, in a 37∘C humid incubator.

Fibrinogen labeling

Alexa Fluor 546 carboxylic acid, succinimidyl ester (Invitrogen) was mixed with fibrinogen solution in a 7.5:1 molar ratio for 1 hour at room temperature and then filtered through a HiTrap desalting column (GE Healthcare) packed with Sephadex G-25 resin, to separate the unreacted dye.

3D fibrin gel preparation

GFP-Actin 3T3 fibroblast cells (8x103 cells) were mixed with 10 µl of a 20 U/ml thrombin solution (Omrix Biopharmaceuticals). Then, 10 µl of a 10 mg/ml fluorescently labeled fibrinogen (Omrix Biopharmaceuticals) suspension was placed in a 35-mm cover-slip bottom dish (MatTek Corporation) and mixed gently with the 10 µl cells suspended in thrombin. The resulting fibrin gel was placed in the incubator for 20 min to polymerize, after which, a warm medium was added to cover the gel. The fibrin gels had an approximate shape of half a sphere, attached to the bottom surface of a cover slip, with a gel height of about 2-3 mm, and cells were fully embedded in the 3D gel. From this point on, the gels including the cells embedded in them, were maintained in 37°C 5% CO^2.

Time-lapse confocal microscopy

Pairs of cells were imaged with a Zeiss 880 confocal microscope, equipped with a 40X NA=1.1 water immersion lens (Zeiss) and an 30mW argon laser was used to image both the cells (GFP-Actin) and the fluorescently labeled-fibrin matrix with excitation wavelength of 488, and a

separated emission spectrum for each. Throughout imaging, the gels with the contained cells were maintained in a 37°C 5% CO_2 incubation chamber. Confocal z-stacks were acquired every 5-15 min for about 6 hours from cell seeding. Confocal imaging inherently includes a tradeoff between the temporal resolution, the axial resolution and the number of imaged locations: higher temporal/axial resolution leads to the lower numbers of locations imaged leading to smaller numbers of communicating cell pairs per experiment. Experiments were imaged in three settings: (1) Temporal resolution of 15 minutes, with 21 locations of images in resolution of 512X512 pixels (0.41X0.41X2 μm in X'Y'Z') and 36 Z-slices. (2) Temporal resolution of 5 minutes, with 9 locations in each and resolution of 256X256 pixels (0.83X0.83X2 μm in X'Y'Z') and 40 Z-slices. (3) Temporal resolution of 21 minutes, with 7 locations of images in resolution of 512X512 pixels (0.41X0.41X0.53 μm in X'Y'Z') and 187 Z-slices, where X', Y' and Z' are the microscopy axes.

Image analysis and quantifications

Preprocessing live imaging data

We first applied Fiji's[31] "Bleach Correction" on the raw fiber channel with the "Histogram Matching" option. On the actin (cell) channel we applied a median filter (radius = 2) followed by a Gaussian blurring filter (sigma = 2), before segmenting the cells over time using the "3D Objects Counter" Fiji's plugin[49] (Threshold = 15, Size filter > 400). The cell's center coordinates in 3D for each time frame was recorded and used for cell tracking. Custom Python code was used for the cell tracking, by identification of cells to track in the first time frame and simply assigning the nearest cell (in 3D Euclidean distance) in the next time frame to construct the trajectory. Shorter trajectories were recorded for cells that moved beyond the field of view during imaging. This simple approach was sufficient thanks to the sparsity of the cell seeding.

Transforming 3D images for visualization and quantification

To visualize and quantify the 3D band between a cell pair we transformed the image to a new coordinate system that is defined in relation to the spatial relation between the pair. We transformed the image from the microscopy axes (denoted X',Y',Z') to the following three new axes. The connecting axis, defined by the line connecting the cells' centers (Fig. S1 and Video

S1 black line). The Z axis, parallel to the microscopy axial plane (Z') and perpendicular to the connecting axis (Fig. S1 and Video S1 cyan line). The XY axis, perpendicular to the connecting axis and to the Z axis (Fig. S1 and Video S1 purple line). For visualization, we used the new 2D axis defined by XY and Z (Fig. S25C). We used Fiji's[31] "Reslice" function (default "Output spacing", "Slice count" according to the fibroblast diameter of 15 µm) to slice the images from top to bottom in the XY axis perpendicular to the connecting axis between the cells, with a width of 15 µm, interpolating axial pixel values to match the spatial resolution in XY using bilinear interpolation. Finally, we averaged the pixel intensities across the slices using Fiji's "Z project" (Projection type = "Average intensity") to create the 2D visualization (for example see the bottom of Fig. 1E). To visualize single cells, we picked an arbitrary XY axis (either 0°, 45°, 90° or 135°) with the same axial axis (Z). These visualizations were used for all experiments and all manual annotations (identifying imaging artifacts, and cell pairs with/without a visible band).

We implemented custom Python code to quantify the ECM density between a pair of communicating cells. First, we transformed the 3D axes to XY slices and Z, replicating the visualization without the Z-interpolation and without the slices averaging. Second, we performed another transformation, rotating the image onto the connecting axis between the cells to reach a common Z-axis. This transformation generates a 3D image where the Z-axis is perpendicular to the XY-axis that is perpendicular to the connecting axis between the cell's centers. This property allows us to move axially in relation to the 3D line connecting the cells. The whole process is depicted in Fig. S25C.

The second transformation rotated the original X', Y' and Z' axes thus defining a new coordinate system, where the transformed pixel size ("resolution") in the new connecting axis and in the Z axis are a weighted combination of the original microscopy resolution in X', Y' and Z'.

$ConnectingAxis_{resolution} = \frac{\theta}{90} * Z'_{resolution} + \frac{90-\theta}{90} * X', Y'_{resolution}; Z_{resolution} = \frac{\theta}{90} *$

$X', Y'_{resolution} + \frac{90-\theta}{90} * Z'_{resolution}, 0 \leq \theta \leq 90$), where θ is the calculated rotation angle between the connecting axis and the microscopy lateral plane before the rotation. The XY axis resolution remains unchanged ($X', Y'_{resolution}$). These new resolutions were used to calculate the size and location of the quantification window (see below).

Single cells do not have a preferred axis in 3D since they do not have a communicating partner. Thus, to quantify ECM density near single cells we sampled around each cell in 32 different

orientations in 3D. 16 transformations were defined using all paired combinations of four angles (0°, 45°, 90° and 135°), each transformation pair was applied similarly to the transformations in cell pairs. For example, the pair <45,135> implies first rotating the image in 45° in X',Y' (blue arrow in Fig. S25D) followed by a 135° rotation in Z' (green arrow in Fig. S25D). These 16 transformations were used in two directions along the rotated axes leading to 32 orientations for quantification (see below).

Manual filtering of defected image frames

A small fraction of frames in a few experiment locations had imaging-related artifacts that hampered our ability to accurately segment the cell and quantify ECM densities. These artifacts included incorrect cell segmentation, dark areas due to imaging malfunctioning of the microscope and "light waves" (Video S13) that may have been the result of an air or water bubble trapped in the lenese's immersion oil. To include these experiments in our analysis we manually identified and recorded defected frames that had these artifacts and considered only valid time frames (without this artificant), when computing fiber density and correlations.

Manual annotation of cell pairs with or without a visible band of increased density

For analysis we considered cell pairs with pair distance ranging at 60-150 μm (4-10 cell diameters, assuming fibroblast diameter of 15μm). Based on previous studies that focused solely on cell pairs with a visible band of increased density between them[7,9,10,50], we partitioned our dataset to cell pairs that formed and ones that did not form a visible band of denser fibers between the cells. This partition was performed manually by visual assessment of the pixel intensity along the full length of the connecting axis between the cells at the end of imaging. Visually apparent bands appeared in approximately 60% of the imaged cell pairs.

Quantification window size

To quantify the local ECM density we used a quantification window of the size of a cell diameter in all axes, in 2D simulations (0.08 AU) or 3D in experiments (15 μm). This size was set to optimize the tradeoff between including sufficient data versus too much irrelevant data within the window. The number of pixels defining the quantification window (cell diameter in simulations, 15 μm in experiments) were calculated according to the transformed image resolutions. The same scale was also used upon shifting the quantification windows.

Quantifying local fiber density in simulations

The local fiber density was calculated as the accumulated fiber volume within the quantification window. We assume that the fiber volume is preserved even when the fiber is deformed. However, this property does not hold in the simulated 2D representation of the fibers where their buckling property reduces the simulated fiber lengths. This is an inherent limitation of simulating a 3D process in 2D. To overcome this limitation we normalize each fiber to its initial length before summing the fiber length in the quantification window. More specifically, we considered two scenarios (Fig. S25E). (1) For the case where the fiber was located exclusively within the quantification window, its length at the onset of the simulation was used for quantification. (2) For the case where the fiber was not located exclusively within the quantification window (i.e., crossing the window boundaries), we used only the sub-fiber within the quantification window while adjusting to the full fiber length at the onset of the simulation: $Fiber_{Volume}(t) = Fiber_{InnerLength}(t) * \frac{Fiber_{Length}(t_0)}{Fiber_{Length}(t)}$, where $Fiber_{Volume}(t)$ is the fiber volume at time t, $Fiber_{InnerLength}(t)$ is the length of the sub-fiber within the quantification window at a time t, $Fiber_{Length}(t_0)$ is the overall fiber length at the onset of simulation and $Fiber_{Length}(t)$ is the overall fiber length at time t.

The fiber density within a quantification window was defined as the accumulated fiber volume within it. For single cells the mean fiber density of four windows, above, below, to the left and to the right of the cell was recorded (Fig. S25F).

Quantifying local fiber density in experiments

The mean fluorescent fibrin channel intensity was used as a proxy of fiber density within the transformed 3D quantification windows (see earlier). Quantification windows with over 5% of pixels extending beyond the image boundaries were marked as "invalid" and were excluded from further analysis. Quantification windows for single cells were calculated similarly to simulations, but in 3D, averaging the mean intensity in 32 orientations (see earlier).

Normalizing the local fiber density in simulations and experiments

To enable quantitative comparison across experiments and between simulations and experiments, we normalized the fiber density to its z-score - the number of standard deviations away from the mean background fiber density at quantification windows that were not influenced by the cells.

Background quantification windows were defined for every location at the onset of simulation/imaging before (simulation) or where minimal (experiments) ECM remodeling occured. To calculate the mean background fiber density we considered all quantification windows that did not intersect with the quantification window around the cells' center (Fig. S25G - simulations, windows step resolution = 0.02 cell diameter in each axis; Fig. S25H - experiments, windows step resolution = 1/10 of the image axis length for each axis). The mean (μ) and the standard deviation (σ) of all background quantification windows was calculated per simulation/location and was used to normalize each quantification window according to the z-score measure, $FiberDensity_{Z-score} = \frac{FiberDensity - \mu}{\sigma}$, i.e., the variation from the mean background intensity in units of standard deviation, where $FiberDensity$ is the fiber density quantification before normalization. This measure could be pooled and compared across locations, experiments and could even be used to compare simulations to experiments.

Extracting local ECM density over time

After performing the image transformation (see above), the quantification windows were placed adjacent to cell boundaries in 2D (simulations) or 3D (experiments) within the cuboid along the connecting axis between the cells, see Fig. 2, Fig. S1 and Video S1. This location was updated at each time frame according to the current cell boundary positions that changed due to cell contraction (simulations) or motion (experiments). Shifts in the quantification windows were performed relative to this position (Fig. S15). Offset in the Z axis translated to a quantification window placed above/below the pair connected axis and perpendicular to the XY axis. Offset in the XY axis translated to a quantification window placed to left/right in XY without changing the Z position. Shifting the quantification window toward the communication partner or away from a single cell (window distance > 0) was performed on the connecting axis between the cells (Fig. S3A), or the axis defined by the image transformation angle in single cells. For a given time-lapse sequence we recorded and normalized the fiber density within the corresponding quantification windows over time. These ECM density time series were used for all correlation-based analyses.

We marked quantification windows within the time series as *invalid* if one of the following criteria holds: (1) Frames with annotated imaging artifacts within the corresponding imaging locations (bad cell segmentation, malfunctioning of the imaging microscope and "light waves",

Video S13). (2) Overlapping quantification windows (for inner correlation analysis), and the future corresponding time frames in the time series (Fig. S25I). (3) Quantification windows with over 5% of pixels extending beyond the image boundaries (Fig. S25J).

Correlation-based analyses

For correlation-based analysis we considered the longest sub-sequences with continuous valid time frames and mutual timestamps (Fig. S25K). We considered only pair cells with mutual sub-sequences of at least 15 (temporal resolution = 15 minutes) or 50 (temporal resolution = 5 minutes) time frames. Correlation was calculated for the second derivative (simulations) or first derivative (experiments) of the fiber density dynamics according to stationarity criteria to avoid high correlations stemming from the monotonic increase of the fiber density (simulations and experiments) and its derivative (simulations) (Fig. S5, Fig. S8). This detrending also dampened the outer correlations so non-communicating outer regions will have no notable correlations. We determined the first/second derivative detrending according to two stationarity tests Kwiatkowski–Phillips–Schmidt–Shin (KPSS)[51] and Augmented Dickey Fuller (ADF)[52]. The null hypothesis in the KPSS test is time series stationarity, while in the ADF test is time series non-stationarity. Temporal correlations were calculated using Pearson correlation on the derived time series. For a cell pair, we defined the *inner correlation* as the temporal correlation between the inner quantification windows adjacent to each cell along the band (Fig. 3A). Inner correlations were used to quantify *cell-ECM-cell communication*.

Same-versus-different pair analysis

To establish that cell-ECM-cell communication of one cell pair can be distinguished from a second cell pair we tested whether the inner correlation between a cell pair ("same" pair) surpassed the correlation between one cell from that pair and another cell from a different cell pair ("different" pair) (Fig. 4A). This comparison was termed *same-versus-different pair analysis*. In this analysis, we considered all combinations of triplets of cells in an experiment, that included one communicating cell pair and another cell that takes part in another communicating pair (Fig. 4A). The quantification window of each cell in the analysis was always located in relation to its communication partner (Fig. 4A).

Pooling data across experiments for statistical assessment

Each experiment was analyzed independently to avoid erroneous relations stemming from correlating two cells in different fibrous networks. Such correlations would be inherently lower when correlating ECM fluctuations between different networks versus in the same fibrous network, due to global network remodeling. Thus, correlating ECM fluctuations between different experiments will lead to erroneously optimistic results, which we avoided here by considering all possible combinations of "same"/"different" for each experiment independently. After analyzing each experiment independently we pooled all the results across experiments for statistical assessment. The non-parametric Wilcoxon signed-rank test was used for statistical analysis testing the null hypothesis that a distribution, such as of "same"-"different" correlations, was distributed around zero.

Controlling for potential masking of cell-ECM-cell communication by local ECM remodeling fluctuations

To verify that our results in the same-versus-different pair analysis were not merely an artifact of local ECM correlations in the fibrous network, we compared the inner correlation of communicating cell pairs to ECM remodeling correlations in quantification windows that were placed in cell-free, fibrous areas. The intuition behind this control experiment was to consider correlations in quantification windows that measure the proximity-component, or the local mutual ECM fluctuations, without the influence of the communicating cells. These controls were performed by manually annotating "fake" cell pairs, and analyzing them in two modes which we termed "static" (Fig. S13C, shadow-less cyan cells) and "following" (Fig. S13A, cyan cells). The quantification windows' locations in the "fake-static" pairs was fixed (Z-axis was arbitrarily set to the middle image Z-slice) while the "fake-following" pair followed its corresponding cell pair motion by shifting in X' and Y' while maintaining a fixed distance from the real pair. "Fake following" pairs showed higher correlations (Fig. S13B versus Fig. S13) and thus had the stronger masking effect for the actual cell-ECM-cell communication validation. Thus, the ultimate control was demonstrated by same-vs-different pair analysis using cell pairs and their corresponding "fake-follower" pairs (Fig. S14).

Assessing sensitivity to temporal resolution

To examine the sensitivity of our method to the temporal resolution we performed same-versus-different pair analysis for down-sampled time series. For the sake of completeness, all possible

38

starting time frames were considered when setting the first time frame for sampling. For example, when down-sampling the temporal resolution from 5 to 15 minutes per frame, there are $15/5 = 3$ possible starting time frames: t_0, t_1 and t_2. When choosing t_1, for example, the first 3 sampled time frames are t_1, t_4, t_7. Time series shorter than 5 (temporal resolution = 15 minutes) or 15 (temporal resolution = 5 minutes) time frames were excluded from further correlation-based analysis. The initial chosen time frame for sampling was set for all same-versus-different computations of that time frame. For each temporal resolution, we pooled all same-versus-different results, which included multiple time series per down-sampled time series as described above. See Fig. S12 for full assessment.

Matchmaking analysis

For each cell that takes part in a cell pair (with a band, or a "fake" pair) we tested our ability to identify its matched communication partner from the local ECM remodeling fluctuations from all the other cells in that experiment. This was performed by ranking the ECM remodeling correlations to all other cells and recording the true communication partner ranking (Fig. 6A). A cell without a valid communicating partner correlation or a sufficiently long time series was not considered as a "pivot" (i.e., the cell that its communication partner is searched for) for matchmaking, but might be considered as a potential communication partner for other "pivot" cells in the matchmaking analysis. Thus, each "pivot" cell had a different number of potential partners and we reported the mean number of potential partners per cell (Fig. 6).

Leader-follower analysis with cross-correlation

Finite-element simulations with a predefined leader and follower were examined using cross-correlation analysis, measuring the correlation between two time series under different time lags. We generated simulations where one cell in a pair was predetermined as the "leader" and its communication partner as the "follower". The "follower" cell "imitated" the "leader" cell contraction in the previous time step, thus the contraction of the "follower" cell is lagging one simulation round behind the "leader". The magnitude of influence that the leader had on the following was defined with the parameter α: $Contraction_{follower}(t) = (1 - \alpha) * N(\mu, \sigma) + \alpha * Contraction_{leader}(t - 1)$, where $t > 1$, $\alpha = 0, 0.25, 0.5, 0.75$ or 1, $\mu = 1$, $\sigma = 0.5$, and $Contraction_{leader}$ was drawn from the normal distribution $N(\mu, \sigma)$. The parameter α indicates

the "followership" magnitude, higher values of α imply that the follower is more influenced by its leader contraction.

In a second simulation we tested whether our approach can identify "leader" and "follower" even when the "follower" contracted more than the "leader", but was still copycating the leader's contraction with a time lag of 1 simulation round. The fold increase of the "follower's" contraction was defined using a parameter β: $Contraction_{follower}(t) = \beta * Contraction_{leader}(t-1)$, where $\beta = 1, 1.05, 1.1 \ or \ 1.2$.

Cross-correlation analysis was performed by comparing different time-lags to the cells' time series and evaluating in relation to the simulation ground truth. Cross-correlation was also performed on experimental data, where ground truth was not available, but did not identify any leader/follower relations, either due to lacking temporal resolution or lack of leaders/followers in our dataset.

Leader-follower analysis with Granger Causality

Granger causality (GC)[53], is a statistical test used to determine whether one time series can significantly contribute to the forecasting of another time series, beyond a base model inferred from the other time series alone and vice versa. GC is an asymmetric measure and was applied twice for each cell pair to test the hypothesis that one cell is influencing its communication partner. We used a multivariate version of the Granger causality test by fitting a vector autoregressive model (VAR) to the time series. The analysis was made on the higher temporal resolution experiments with 5 minutes between consecutive time frames with at least 80 time frames, because experiments at lower temporal resolution did not include sufficient time frames for GC analysis. We performed the following steps: (1) Testing for stationary. Kwiatkowski–Phillips–Schmidt–Shin (KPSS)[51] and Augmented Dickey Fuller (ADF)[52] tests, with p-value < 0.05, on the first derivative of the fiber density time-series. These tests were used to determine whether a time series was stationary around a deterministic trend, a required property for GC. The null hypothesis in the KPSS test is that the time series is stationary, while in the ADF test the time series is non-stationary. Only time series that passed both tests were considered for further analysis. (2) Building a vector autoregression (VAR) model. Based on those time series we created a VAR model using Python "statsmodels"[54] library. (3) Finding the correct time lag. Using the "select_order" function of the VAR model we retrieved 4 possible lags according to

AIC, BIC, FPE and HQIC estimators, of those we selected the minimal lag. (4) Training the model. We trained the VAR model using the "fit" function with the minimal lag we found. (5) Checking for no autocorrelation in the residuals. By testing for whiteness with p-value < 0.05 using the "test_whiteness" function of the fitted model results we filtered out time series that did not pass the test. This function tests the residuals for autocorrelations different from zero, where the variance of the errors is not constant ("whiteness test"), using the Portmanteau test[55]. (6) Checking for Granger Causality. Using the "test_causality" function in the fitted model we tested the time serieses for GC with p-value < 0.05. We reported the statistical significance of each GC test at confidence level of 0.05, without multiple hypotheses correction, and after FDR[33] multiple hypotheses correction at 0.15 (which is considered reasonable in many domains).

Out of 73 cell pairs included in this analysis 14 were with a visible band. 21 of the pairs passed the Whiteness test (2 with a band), 5 of them passed the GC test (1 with a band); Four pairs were found with one-directional causality and another pair with bi-directional causality of both cells of the pair. The fact that we found 6 out of 42 significant GC tests (Fig. 7F), almost 3-fold beyond the randomly expected 5% (= 2.1) increase our confidence that at least some of these pairs hold true leader-follower relations. Further experiments are required to establish this result.

Data

See Table S1 for detailed information regarding all simulated and experimental data in this work.

Software and data availability

We are currently organizing our data and source code and will make both publically available as soon as possible. This data will include the raw simulated and image data with their corresponding metadata, the processed ECM remodeling fluctuation time series, and code to perform our analyses.

Supplementary figures
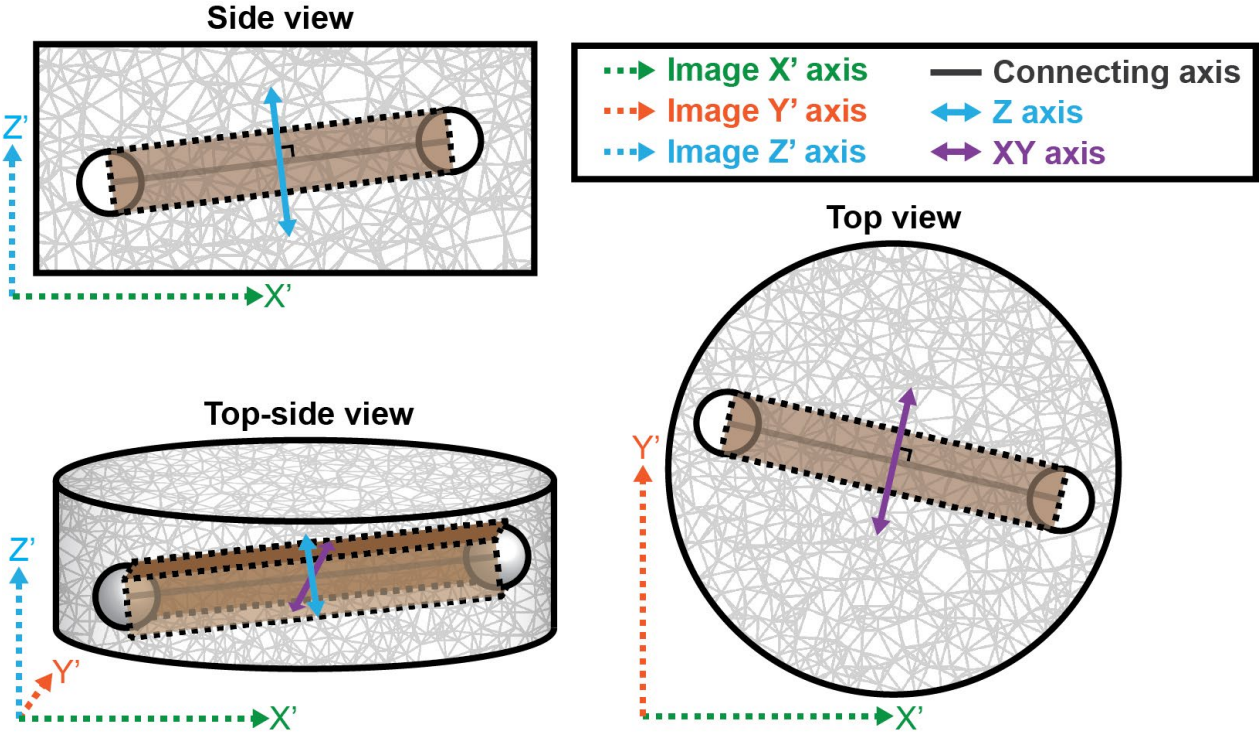
Figure S1: ECM remodeling dynamics are quantified along the connecting axis between the cells. Microscopy axes (X', Y', Z') marked with dashed arrows, transformed visualization and quantification axes (connecting axis, XY, Z) marked with solid arrows. The cuboid region in-between the cell pair (brown), has the width of a cell diameter, and is used for quantification along the connecting axis. The length of the cuboid region is the pair distance. The cuboid left and right sides were parallel to the microscopy axial plane. The Z-axis (cyan) and the XY-axis (purple) are perpendicular to each other and to the connecting axis (black).

Figure S2: Quantifying cell-ECM-cell communication as a function of distance between cell pairs. (**A**) Simulations. Pair distan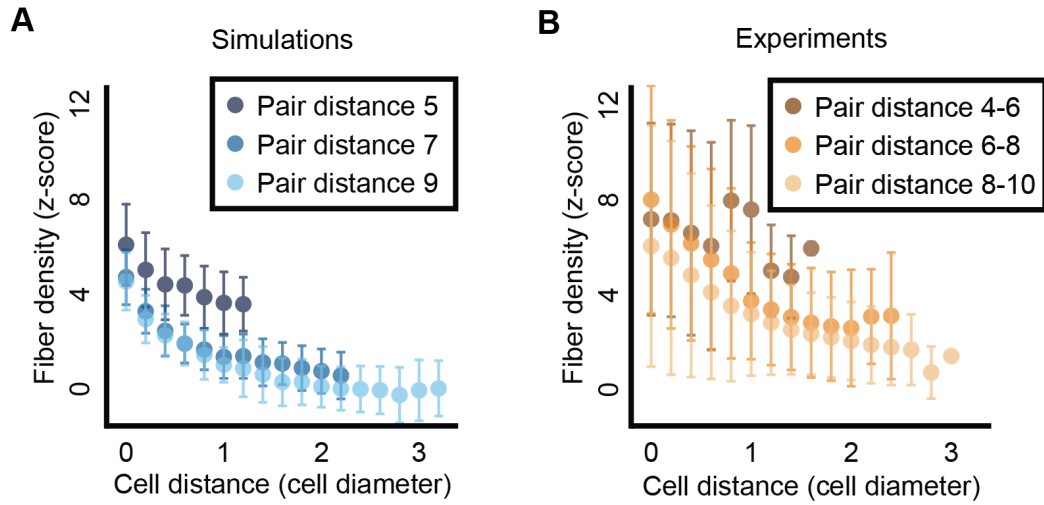ce of 5 (N = 20 pairs), 7 (N = 20 pairs), or 9 (N = 19 pairs) cell diameters. (**B**) Experiments. Pair distance of 4-6 (N = 9 pairs), 6-8 (N = 13 pairs) or 8-10 (N = 5 pairs) cell diameters (assuming cell diameter of 15 μm).

A

Pair distance

Fibers density

Window distance

C

Window distance (cell diameter)	Correlation: pair distance vs. fiber density	N	P-value
0	0.18	54	0.21
0.2	0.1	52	0.48
0.4	0.05	49	0.73
0.6	-0.16	41	0.31
0.8	**-0.37**	**40**	**0.02** *
1	**-0.37**	**38**	**0.02** *
1.2	-0.18	35	0.3
1.4	-0.19	35	0.27
1.6	-0.23	29	0.22
1.8	-0.07	25	0.73
2	-0.11	21	0.64
2.2	-0.37	17	0.14
2.4	-0.41	14	0.14
2.6	**-0.71**	**10**	**0.02** *
2.8	-0.49	6	0.32

B

Fiber density (z-score)

Pair distance (cell diameter)

Correlation: pair distance vs. fiber density

Window distance (cell diameter)

Fiber density (z-score)
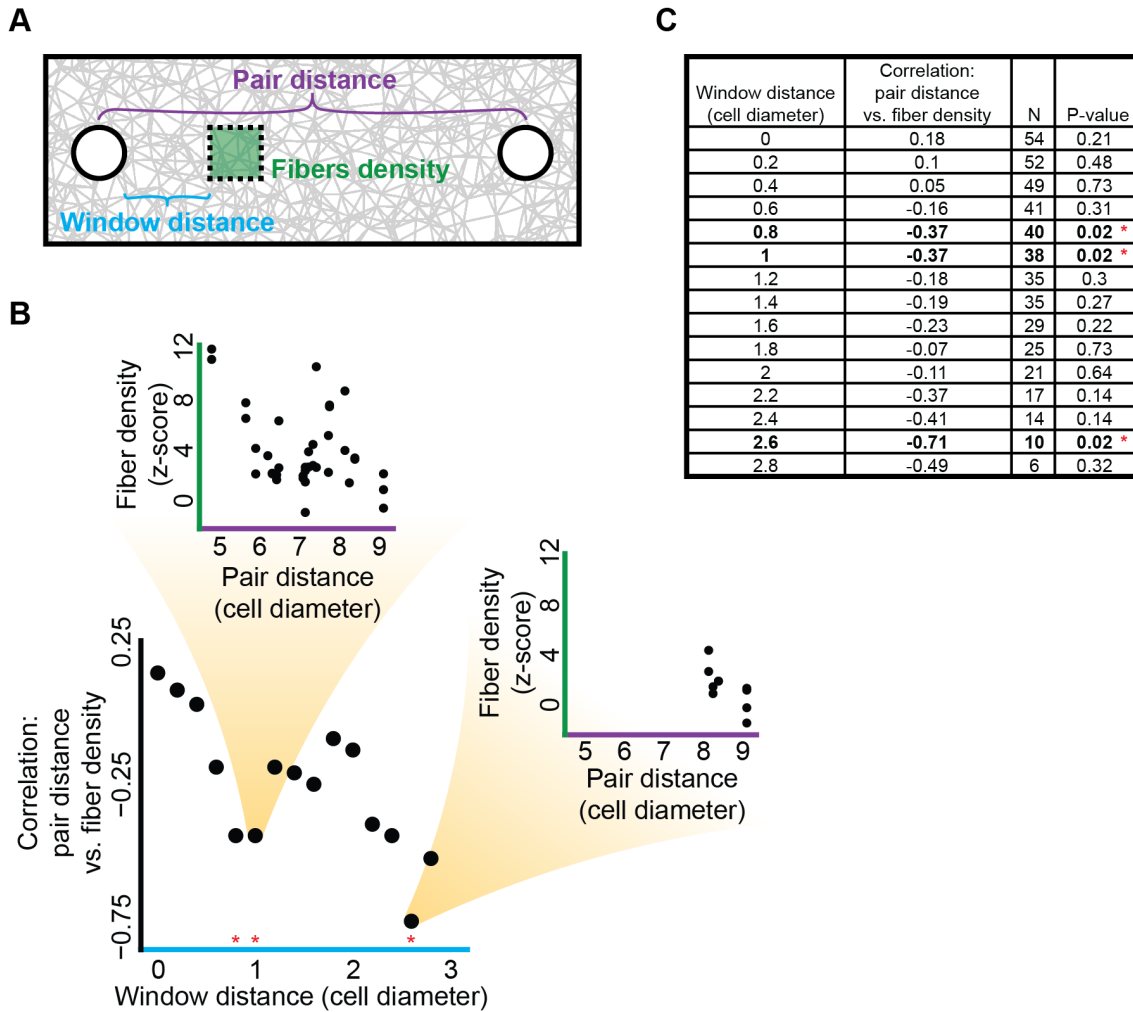
Pair distance (cell diameter)

Figure S3: The distance between pairs of communicating cells is negatively correlated to the density of fibrous regions further away from the cell. I.e., as the quantification region moves away from one cell, the effect of the other cell drops as a function of the pair distance, implying a stronger mechanical interaction with the other cell for closer pairs. (**A**) Schematic sketch. Pair distance (purple) between cell pairs at the onset of imaging. Window distance (cyan) is measured from the boundaries of one cell toward the other cell in the pair, along the axis (in 3D) defined by the pair. (**B**) Correlation between the window distance and the correlation between pair distance and fiber density across cell pairs. N = 15 window distances. Pearson correlation coefficient = -0.76, p-value < 0.001. Red asterisks reflect a significance level below 0.05. Insets: two significant correlations between fiber density pair distance for window distance of 1 (top) and 2.6 (right) cell diameters. N = 38 (top) and 10 (right) communicating cell pairs. Pearson correlation coefficient = -0.37 (top) and -0.71 (right), p-value = 0.02 for both. The reduced number of cell pairs (right) stems from overlapping of the quantification regions due to short pair distances. Note that the color coding (purple, cyan, green) is matching the sketch in panel A. (**C**) Summary table for the data in panel B. Bold rows with red asterisk reflect correlations with significance levels below 0.05.
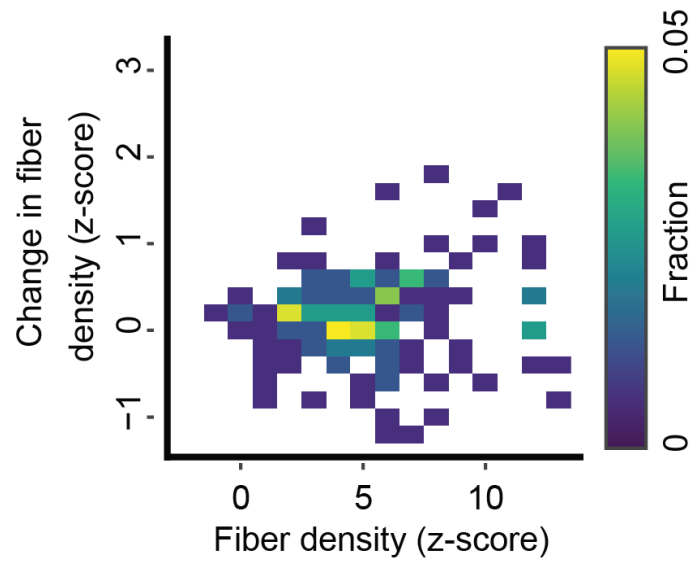
Figure S4: Two-dimensional distribution of fiber density and change in fiber density in consecutive time frames in late (180-270 minutes) stages of the experiment. Quantification windows adjacent to each cell along the band. N = 30 cell pairs in distances between 5 and 10.5 cell diameters (75-157.5 μm). Temporal resolution of 15 minutes between consecutive time frames. Pearson correlation coefficient = 0.16, p-value < 0.05.
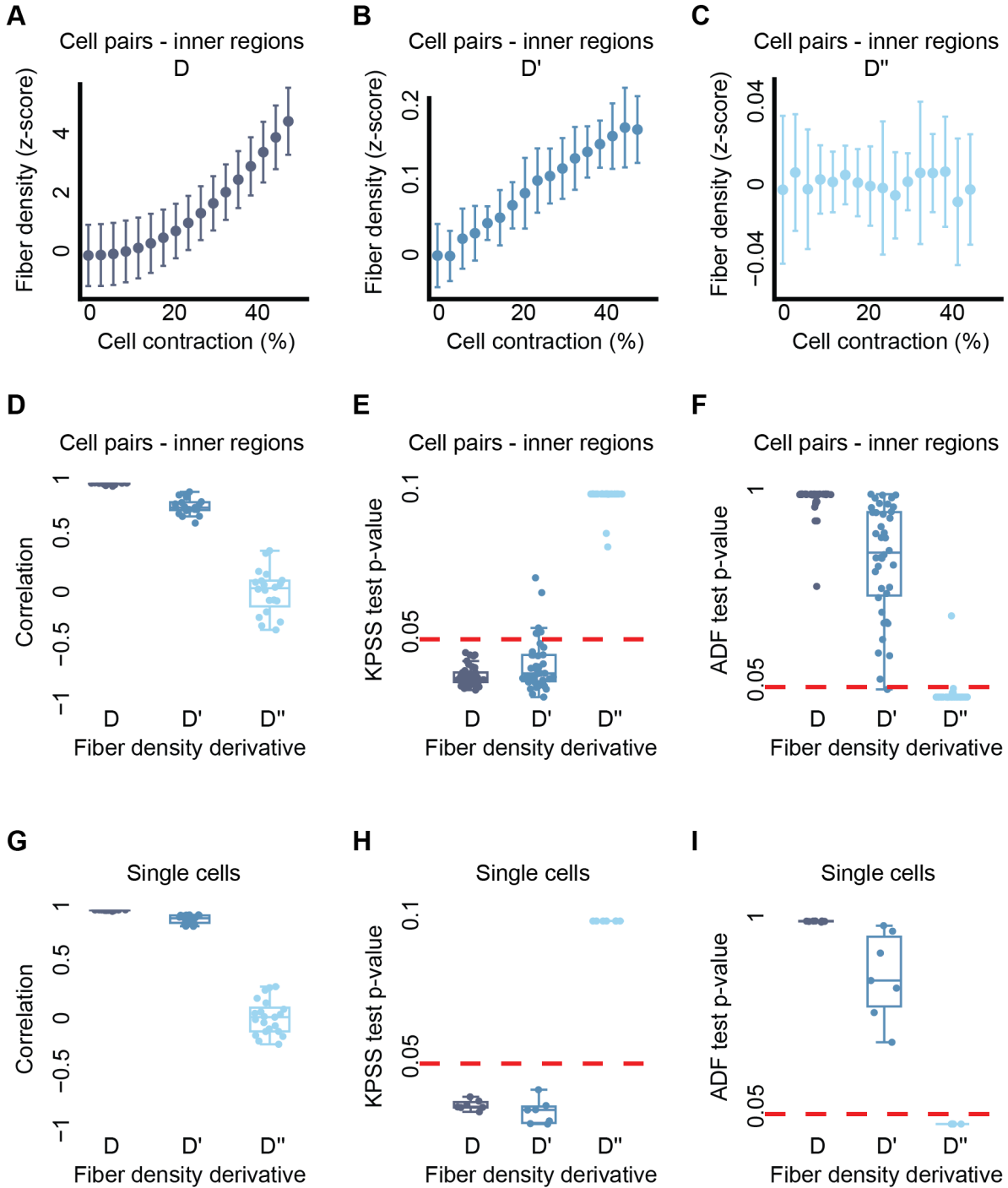
Figure S5: Detrending fiber density dynamics in inner regions of simulated cell pairs and in regions adjacent to simulated single cells. Constant cells contraction of 1% in every time frame. (**A-F**) Cell pairs in distance = 7 cell diameters. N = 20 cell pairs. (**A**) Fiber density dynamics show a clear trend. (**B**) First derivative of fiber density dynamics show a clear trend. (**C**) Second derivative of fiber density dynamics - no obvious trend. (**D**) Inner correlations for fiber density (D), first temporal derivative (D') and second temporal derivative (D''). This panel is a duplicate of Fig. 3B, for figure completeness. Wilcoxon signed-rank testing the null hypothesis that the correlations are distributed around a mean = 0: p-value < 0.0001 (D), < 0.0001 (D') and not significant (D''). (**E**) Kwiatkowski–Phillips–Schmidt–Shin (KPSS) testing the

null hypothesis that the data is stationary. Raw time series (D), first (D') and second derivative (D'') of fiber density dynamics. Each data point is the KPSS test p-value rejecting the null hypothesis that the time series is stationary, with p-value < 0.05. The null hypothesis is rejected for 100% of the raw time series, 85% for the first derivative and 0% for the second derivative. (**F**) Augmented Dickey Fuller test (ADF) testing the null hypothesis that the data is non-stationary. Raw time series (D), first (D') and second derivative (D'') of fiber density dynamics. Each data point is the ADF test p-value rejecting the null hypothesis that the time series is not stationary, with p-value < 0.05. The null hypothesis is rejected for 0% of the raw time series, 2.5% for the first derivative and 97.5% for the second derivative. (**G-I**) Single cells. N = 7 cells. (**G**) Fiber density dynamics correlations between different cells. Correlations are computed between all possible pairs of single cells, total of 21 correlations. Wilcoxon signed-rank testing the null hypothesis that the correlations are distributed around a mean = 0: p-value < 0.0001 (D), p-value < 0.0001 (D') and p-value not significant (D''). (**H**) Kwiatkowski–Phillips–Schmidt–Shin (KPSS) testing the null hypothesis that the data is stationary. Raw time series (D), first (D') and second derivative (D'') of fiber density dynamics. Each data point is the KPSS test p-value rejecting the null hypothesis that the time series is stationary, with p-value < 0.05. The null hypothesis is rejected for 0% of the raw time series, 0% for the first derivative and 100% for the second derivative. (**I**) Augmented Dickey Fuller test (ADF) testing the null hypothesis that the data is non-stationary. Raw time series (D), first (D') and second derivative (D'') of fiber density dynamics. Each data point is the ADF test p-value rejecting the null hypothesis that the time series is not-stationary. The null hypothesis is not rejected with confidence of 0.05, for 100% of the raw time series, 100% for the first derivative and 0% for the second derivative.
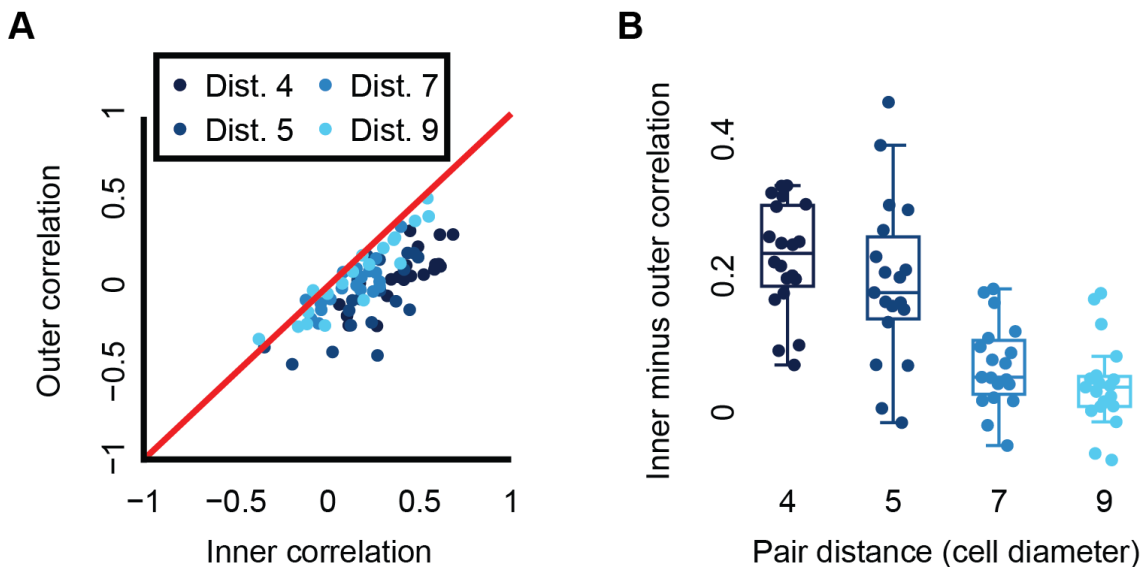

Figure S6: Distinction between matched inner and outer correlations is negatively associated with pair distance (color coded), the distance between pairs of communicating cells. (**A-B**) Inner and outer correlations for pair distances 4 (N = 20 pairs), 5 (N = 19 pairs), 7 (N = 19 pairs) and 9 (N = 19 pairs) cell diameters. Each cell draws its contraction in each step independently from a normal distribution with mean of 1% and standard deviation of 0.5%. Correlations were calculated from the second derivative of fiber density dynamics. Wilcoxon signed-rank testing the null hypothesis that the differences of inner minus outer correlations are distributed around a mean = 0: p-value < 0.0001 (Dist. 4), p-value < 0.001 (Dist. 5), p-value < 0.001 (Dist. 7) and p-value < 0.01 (Dist. 9). (**A**) Inner versus outer correlations. Red y = x reflects the situation where the inner correlation is equal to the outer correlation. (**B**) The distribution

of the deviations of inner from their corresponding outer correlations for each pair distance (subtraction of outer from inner correlations).
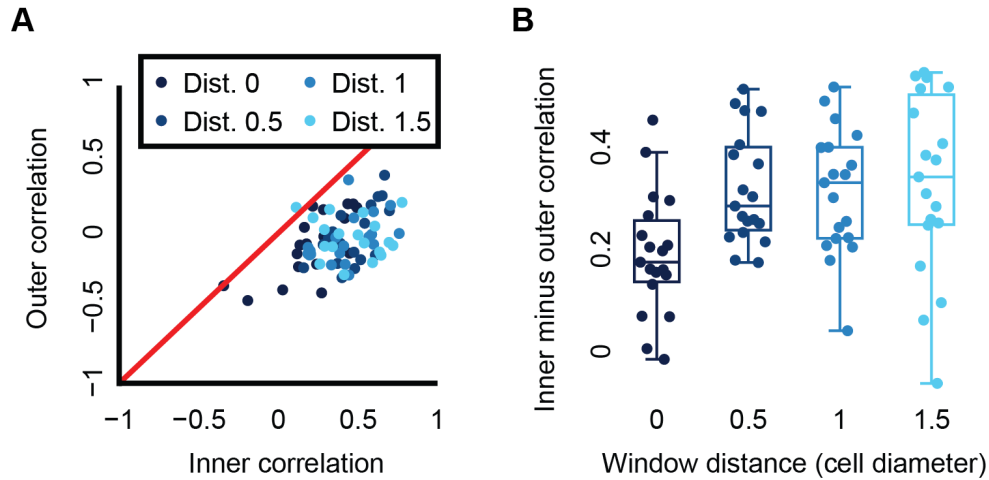

Figure S7: Distinction between matched inner and outer correlations is improved with increased window distance (color coded). Window distance is measured from the boundary of one cell toward the other cell in the pair, along the axis between the pair (Fig. S3A). (**A-B**) Inner and outer correlations for window distances of 0, 0.5, 1 and 1.5 cell diameters. N = 19 cell pairs with pair distance of 5 cell diameters. Each cell draws its contraction from a normal distribution with mean of 1% and standard deviation of 0.5%. Correlations were calculated from the second derivative of fiber density dynamics. Wilcoxon signed-rank testing the null hypothesis that the differences of inner minus outer correlations are distributed around a mean of 0: p-value < 0.001 for all window distances. (**A**) Inner versus outer correlations. Red y = x reflects the situation where the inner correlation is equal to the outer correlation. (**B**) The distribution of the deviations of inner from their corresponding outer correlations for each window distance (subtraction of outer from inner correlations).
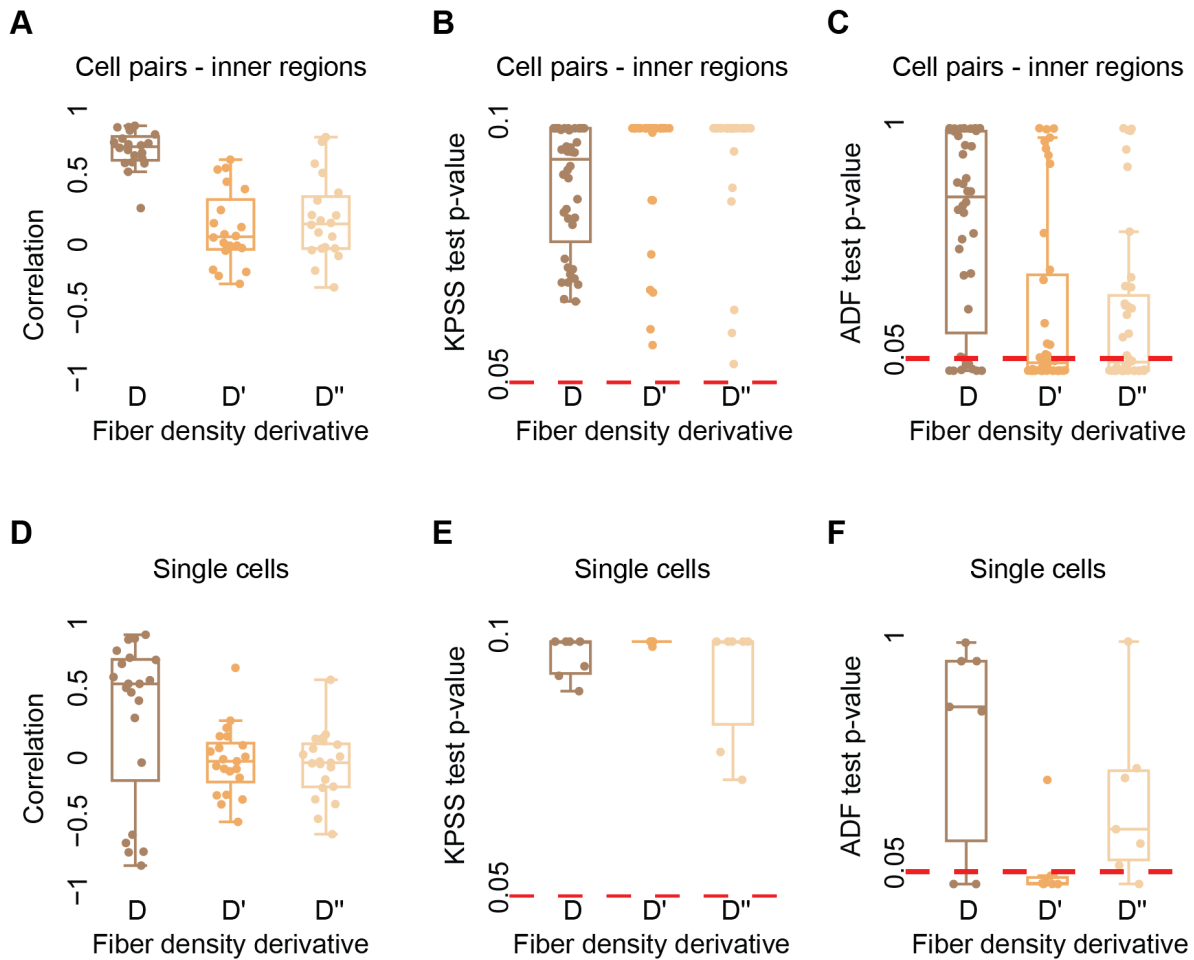
Figure S8: Detrending fiber density dynamics of inner correlation (cell pairs) and of single cell correlations. Inner/single cell correlations for fiber density (D), first temporal derivative (D') and second temporal derivative (D''). (**A-C**) Cell pairs. Pairs distance 60-150 μm (4-10 cell diameters). N = 20 cell pairs. (**A**) Wilcoxon signed-rank testing the null hypothesis that the correlations are distributed around a mean = 0: p-value < 0.0001 (D), < 0.05 (D') and < 0.01 (D''). (**B**) Kwiatkowski–Phillips–Schmidt–Shin (KPSS) testing the null hypothesis that the data is stationary. Each data point is the KPSS test p-value rejecting the null hypothesis that the time series is stationary, with p-value < 0.05. The null hypothesis is rejected for 100% of the raw, first, or second derivative time series. (**C**) Augmented Dickey Fuller test (ADF) testing the null hypothesis that the data is non-stationary. Each data point is the ADF test p-value rejecting the null hypothesis that the time series is not stationary, with p-value < 0.05. The null hypothesis is rejected for 20% of the raw time series, 55% for the first derivative and 55% for the second derivative. (**D-F**) Single cells. N = 7 cells. Correlations are computed between all possible pairs of single cells, total of 21 correlations. (**D**) Wilcoxon signed-rank p-value < 0.05 (D), not significant (D', D''). (**E**) KPSS is not rejected for all raw, first, or second derivative time series. (**F**) ADF is rejected for 28.6% of the raw time series, 85.7% for the first derivative and 14.3% for the second derivative.
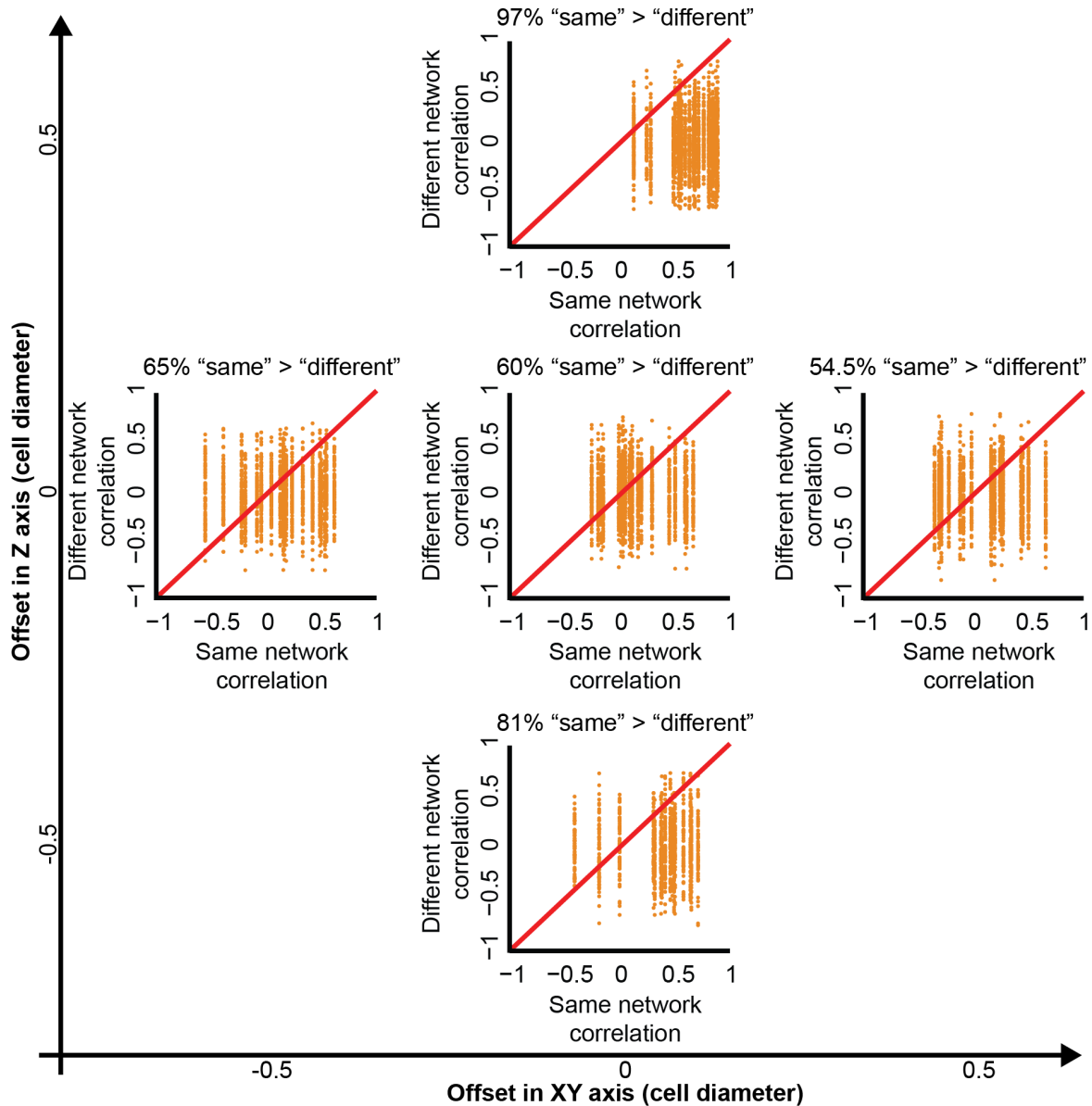
Figure S9: Enhanced identification of communicating cells by shifting the quantification window's location. Same-versus-different pair analysis for different locations of the quantification window. Pair distance was 60-150 μm (~4-10) cell diameters, window distance = 0, correlations were calculated using the first derivative of fiber density dynamics. All combinations of "same"/"different" were considered. Slightly different numbers of cell pairs per quantification window location stems from discarding pairs where the quantification windows exceeded beyond the image boundaries. See Fig. S15 for axes schematics. **Top panel (Z = 0.5, XY = 0)**: N = 25 cell pairs. "Same" pair had a higher correlation than "different" pair in 97% of the matched correlations. Wilcoxon signed-rank p-value < 0.0001. **Left panel (Z = 0, XY = -0.5)**: N = 20 cell pairs. "Same" pair had a higher correlation than "different" pair in 65% of the matched correlations. Wilcoxon signed-rank p-value < 0.0001. **Middle panel (Z = 0, XY = 0)**: N = 20 cell pairs. "Same" pair had a higher correlation than "different" pair in 60% of the matched correlations. Wilcoxon signed-rank p-value < 0.0001. **Right panel (Z = 0, XY = 0.5)**: N = 20 cell pairs. "Same" pair had a higher correlation than "different" pair in 54.5% of the matched correlations. Wilcoxon signed-rank p-value < 0.0001. **Bottom panel (Z = -0.5, XY = 0)**: N = 16 cell pairs. "Same" pair had a higher

correlation than "different" pair in 81% of the matched correlations. Wilcoxon signed-rank p-value < 0.0001.
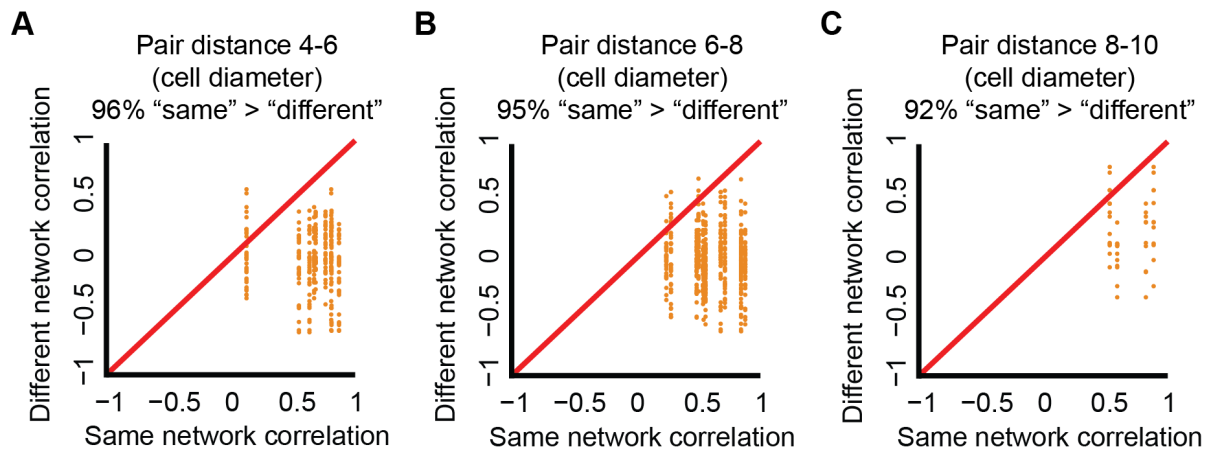

Figure S10: Identification of communicating cells in different pair distances. Same-versus-different pair analysis. Quantification windows were placed 7.5 μm above the connecting axis between the cells (see Fig. 5E for schematics). Correlations were calculated using the first derivative of fiber density dynamics. All combinations of "same"/"different" were considered. Partitioning the data to cell pairs intervals of 4-6, 6-8, or 8-10 cell diameters was performed under the assumption of a mean fibroblast diameter of 15 μm. (**A**) Pair distance 60-90 μm (4-6 cell diameters). N = 9 cell pairs. "Same" pair had a higher correlation than "different" pair in 96% of the matched correlations. Wilcoxon signed-rank p-value < 0.0001. (**B**) Pair distance 90-120 μm (6-8 cell diameters). N = 12 cell pairs. "Same" pair had a higher correlation than "different" pair in 95% of the matched correlations. Wilcoxon signed-rank p-value < 0.0001. (**C**) Pair distance 120-150 μm (8-10). N = 4 cell pairs. "Same" pair had a higher correlation than "different" pair in 92% of the matched correlations. Wilcoxon signed-rank p-value < 0.0001.

A

Cell pairs with band
100% "same" > "different"

B

Cell pairs with no band
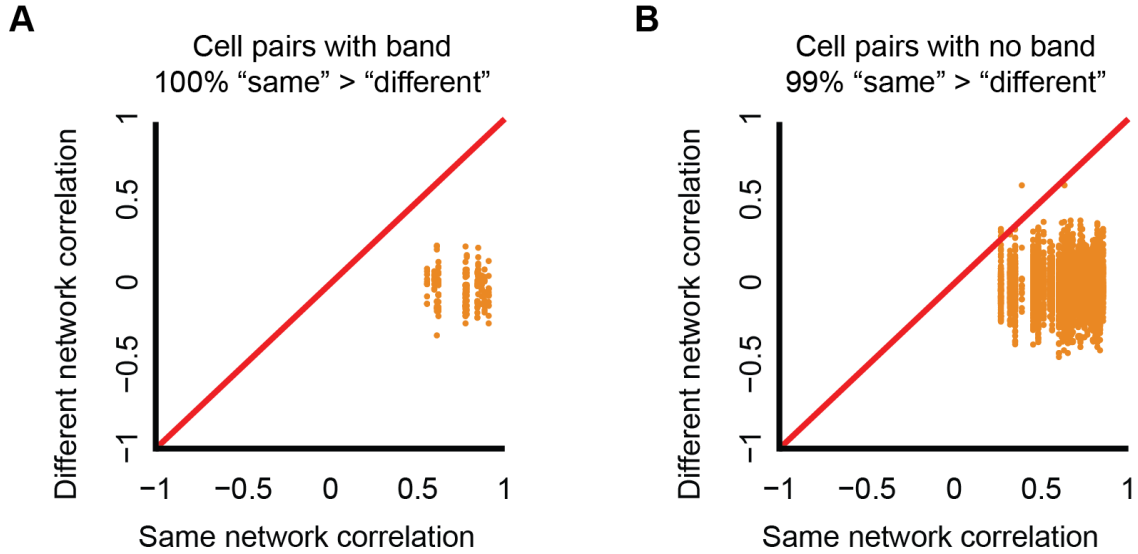99% "same" > "different"

Figure S11: Identification of communicating cells in higher temporal resolution of 5 minutes per frame. Same-versus-different pair analysis. Pair distance 60-150 μm, quantification windows were placed 7.5 μm above the connecting axis between the cells (see Fig. 5E for schematics). Correlations were calculated using the first derivative of fiber density dynamics. All combinations of "same"/"different" were considered. (**A**) Pairs with a visible band. N = 14 cell pairs. "Same" pair had a higher correlation than "different" pair in all (100%) of the matched correlations. Wilcoxon signed-rank p-value < 0.0001. (**B**) Pairs with no visible band. N = 56 cell pairs. "Same" pair had a higher correlation than "different" pair in 99% of the matched correlations. Wilcoxon signed-rank p-value < 0.0001.
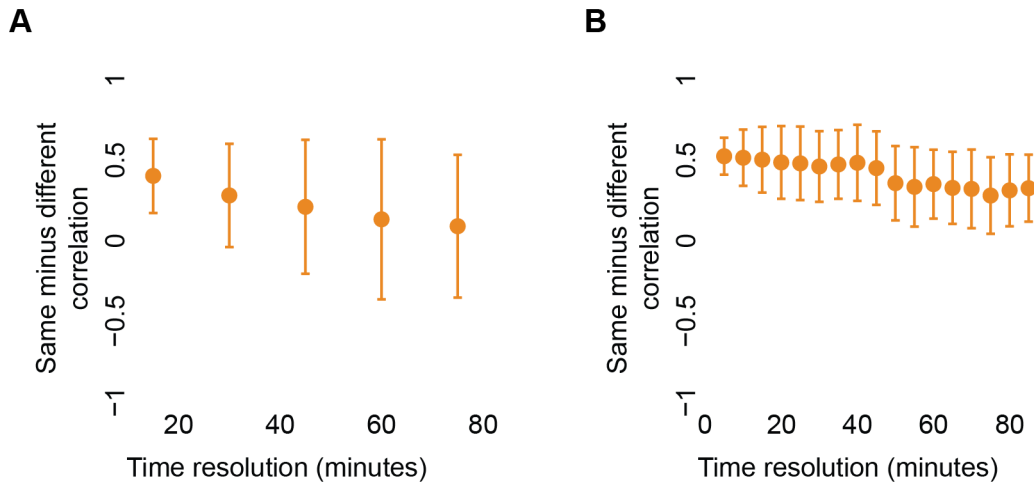

A

B

Figure S12: Sensitivity of same-versus-different pair analysis to the temporal resolution. Pairs distance = 60-150 μm. Quantification windows were located 7.5 μm above the connecting axis between the cells (see Fig. 5D for schematics). Correlations were calculated using the first derivative of fiber density dynamics. The original temporal resolution was artificially down-sampled to multiple time series of reduced time resolutions with different starting times. All possible time intervals under a given temporal resolution (different starting time) were considered leading to multiple recorded observations for a single pair of communicating cells (Methods). (**A**) Low temporal resolution experiments. Original time resolution was

15 minutes per frame. N = 1 experiment. n = 25 pairs (15/30/45 minutes), n = 23 pairs (60 minutes) and n = 14 pairs (75 minutes). "Same" pair had a higher correlation than "different" pair in 96.7% (15 minutes), 84.1% (30 minutes), 70.1% (45 minutes), 63.7% (60 minutes) and 64.5% (75 minutes) of the matched correlations. Wilcoxon signed-rank p-value < 0.0001 for all temporal resolutions. (**B**) High temporal resolution experiments (5 minutes per frame). N = 3 experiments, same-versus-different pair analysis was performed independently for each experiment and the results were pooled together without mixing pairs from different experiments. n total pairs = 14 pairs (5/10/15 minutes, 100/99.1/95.5% correspondingly), n = 13 pairs (20 minutes, 97.8%), n = 12 pairs (25 minutes, 97.9%), n = 9 pairs (30/35/40 minutes, 97/96.3/94.1% correspondingly), n = 8 pairs (45 minutes, 94.7%), n = 5 pairs (50/55/60/65/70 minutes, 92/90.5/91.9/90.4/87.4%), n = 4 pairs (75/80 minutes, 85.3/87.2% correspondingly), n = 2 pairs (85 minutes, 93%).
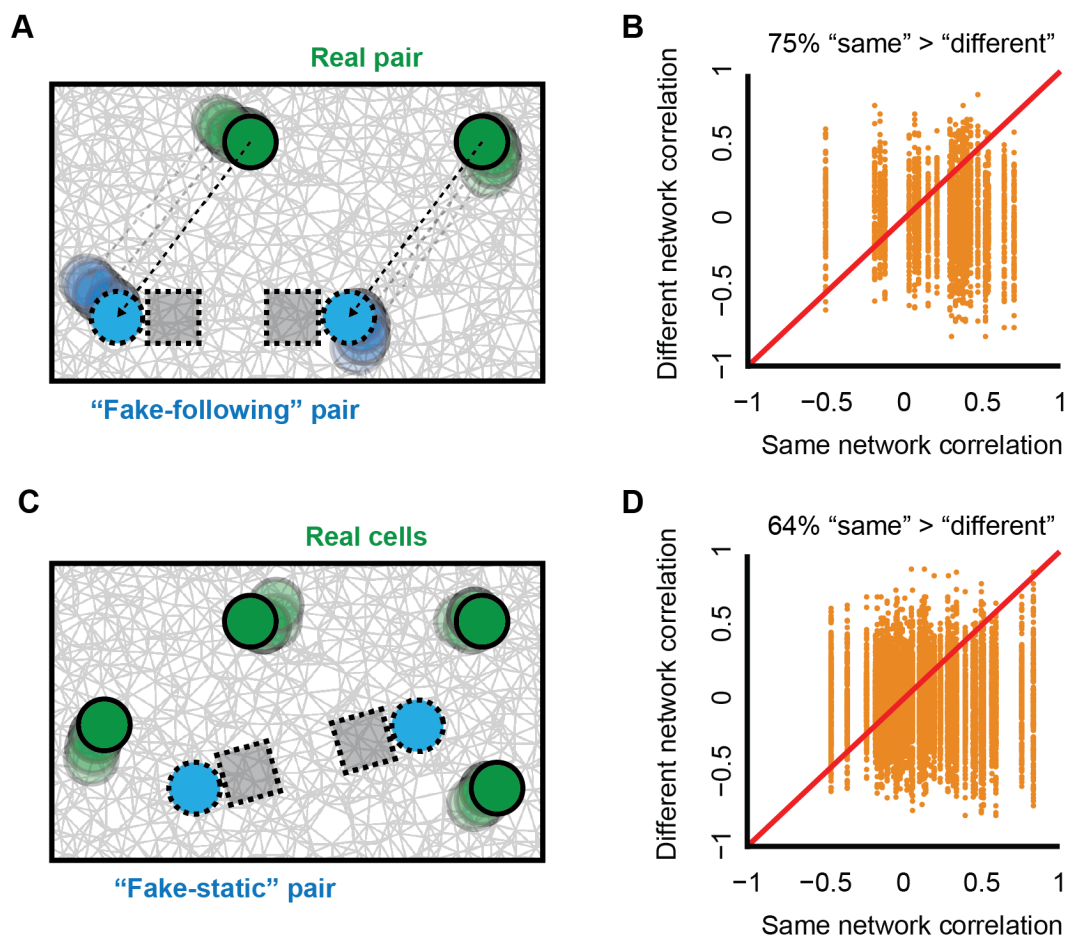

Figure S13: Controlling for potential masking of cell-ECM-cell communication by local ECM remodeling fluctuations. Same-vs-different pair analysis with a "fake" cell pair. Fake cell pairs come in two flavors, "following" (A-B) or "static (C-D) (see Methods). Pair distance was 60-150 μm, the quantification window was defined 7.5 μm above the connecting axis between the (real) cell pair (see Fig. 5E for schematics) and placed in relation to the XY position of the fake cells. Correlations were calculated using the first derivative of fiber density dynamics. (**A**) Schematic sketch of a "fake-following" pair (cyan) mimicking a real cell pair (green) by repeating the cells' shifts in X and Y axes (green shadow) in a fixed distance from the real pair (cyan shadow). (**B**) Quantification of "fake-following" pairs. N = 25 cell pairs. "Same" pair had a higher correlation than "different" pair in 75% of the matched

correlations. Wilcoxon signed-rank p-value < 0.0001. (**C**) Schematic sketch of a "fake-static" pair (cyan), that was manually placed in fixed coordinates (shadow-less cyan) in an ECM region distant from cells (green) in each location of imaging (Methods). (**D**) Quantification of "fake-static" pairs. N = 50 cell pairs. "Same" pair had a higher correlation than "different" pair in 64% of the matched correlations. Wilcoxon signed-rank p-value < 0.0001. The results in panels B versus D show that the cell communication masking effect due to local ECM correlations exists and is more severe in the "fake-following" setting. Thus, the direct assessment of these masking effects on measuring cell-ECM-cell communication in Fig. S14 will focus on the "fake-following" control.

A No offset in Z axis
60%   70%

B No offset in Z axis
46% real > fake

C Offset 0.5 in Z axis
97%   75%

D Offset 0.5 in Z axis
76% real > fake

E No offset in Z axis
High temporal resolution
64%   78%

F No offset in Z axis
High temporal resolution
47% real > fake

G Offset 0.5 in Z axis
High temporal resolution
100%   87%

H Offset 0.5 in Z axis
High temporal resolution
90% real > fake
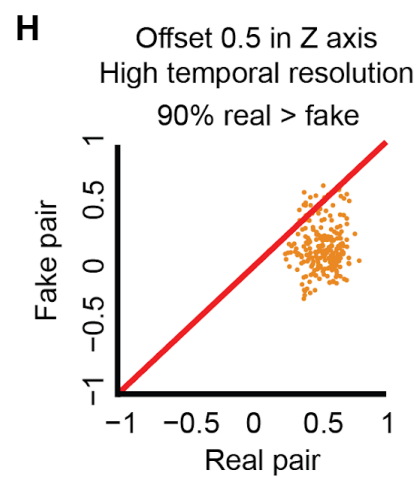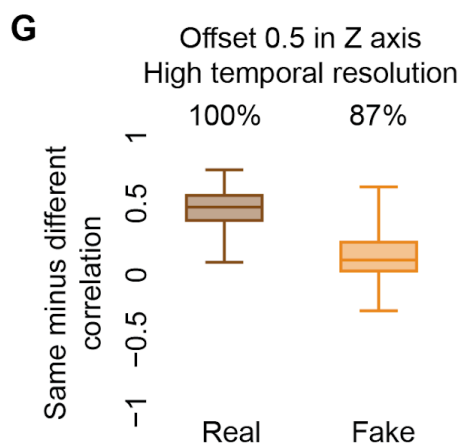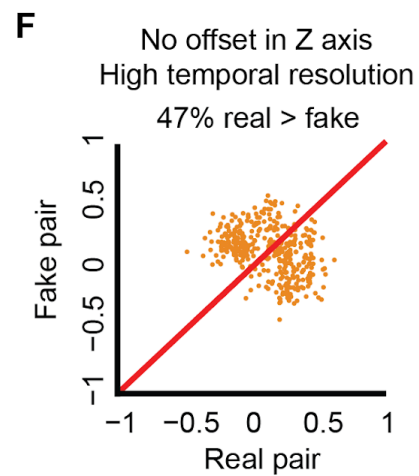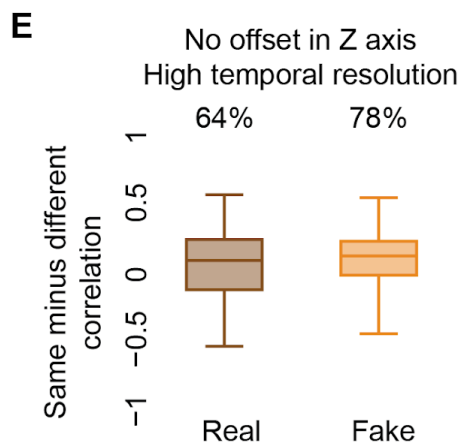
Figure S14: Cell-ECM-cell communication is more prominent than the masking by local ECM remodeling fluctuations. Same-vs-different pair analysis of cell pairs and their corresponding "fake-follower" cell pair (Fig. S13A). "Fake-follower" pairs were used for comparison, and not "fake-static" (Fig. S13C) because they were shown to have a stronger masking effect (Fig. S13). Pair distance 60-150 μm, correlations were calculated using the first derivative of fiber density dynamics. All combinations of "same"/"differ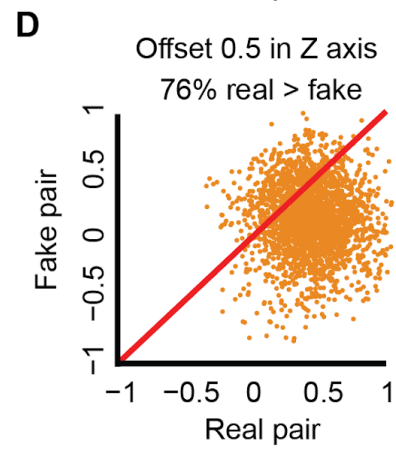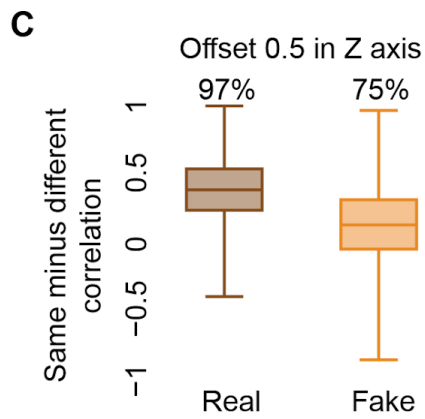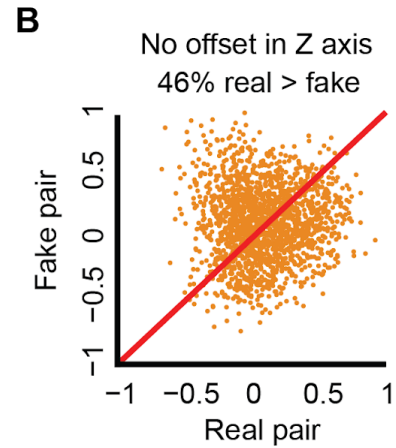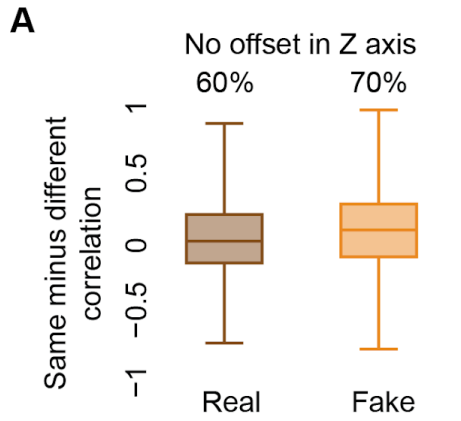ent" were considered for both the cell pairs and the "fake" cell pairs independently. Panels A, C, E, G compare the distribution of same-vs-different pair analysis of cell pairs ("real") versus "fake-follower" pairs ("fake"). Panels B, D, F, G compare matched same-vs-different pair analysis for each cell pair ("real") and its corresponding "fake-follower" pair ("fake"). Panels A-D and E-H are the same analysis with low (15 minutes) versus high (5 minutes) temporal resolution correspondingly. In panels A-B and E-F the quantification window is located at the focal plain between the cell pair, while in panels C-D and G-H 7.5 μm above the focal plain between the cell pair. (**A-B**) Quantification window at the focal plain between the cell pair. Temporal resolution = 15 minutes. N = 20 matched pairs. (**A**) "Same" > "different" in 60% ("real") and 70% ("fake") of the same-vs-different pair analysis observations. Wilcoxon signed-rank p-values < 0.0001. (**B**) "Real" > "fake" in 46% of the matched same-vs-different pair analysis observations. Wilcoxon signed-rank p-value < 0.0001. (**C-D**) Quantification window 7.5 μm above focal plain between the cell pair. Temporal resolution = 15 minutes. N = 25 matched pairs. (**C**) "Same" > "different" in 97% ("real") and 75% ("fake") of the same-vs-different pair analysis observations. Wilcoxon signed-rank p-values < 0.0001. (**D**) "Real" > "fake" in 76% of the matched same-vs-different pair analysis observations. Wilcoxon signed-rank p-value < 0.0001. (**E-F**) Quantification window at the focal plain between the cell pair. Temporal resolution = 5 minutes. N = 19 matched pairs. (**E**) "Same" > "different" in 64% ("real") and 78% ("fake") of the same-vs-different pair analysis observations. Wilcoxon signed-rank p-values < 0.0001. (**F**) "Real" > "fake" in 47% of the matched same-vs-different pair analysis observations. Wilcoxon signed-rank p-value < 0.05. (**G-H**) Quantification window 7.5 μm above focal plain between the cell pair. Temporal resolution = 5 minutes. N = 14 matched pairs. (**G**) "Same" > "different" in 100% ("real") and 87% ("fake") of the same-vs-different pair analysis observations. Wilcoxon signed-rank p-values < 0.0001. (**H**) "Real" > "fake" in 90% of the matched same-vs-different pair analysis observations. Wilcoxon signed-rank p-value < 0.0001.
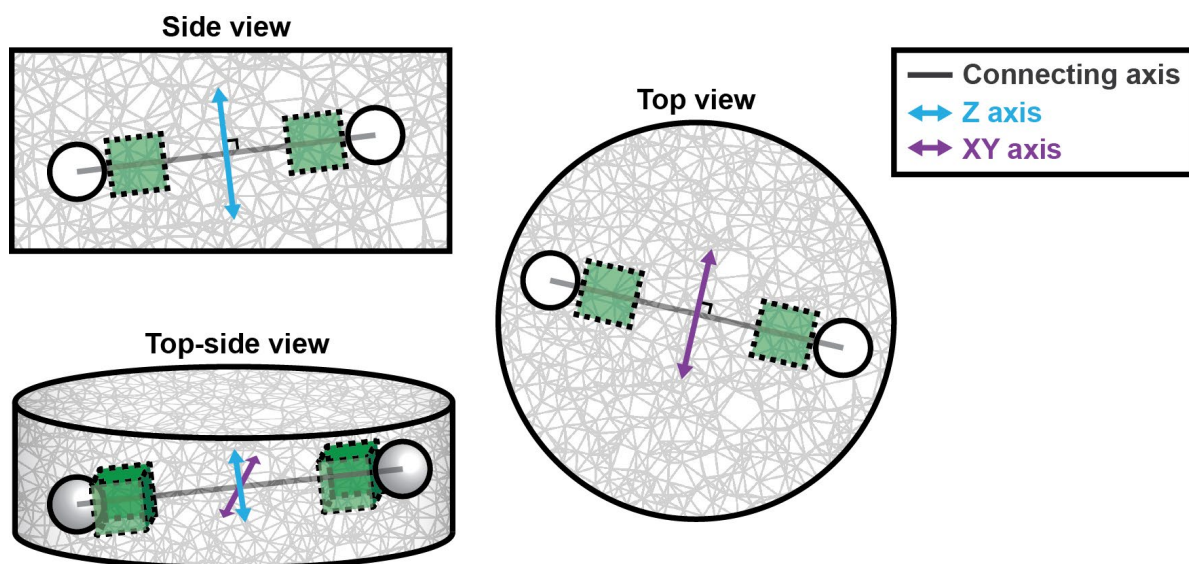

Figure S15: Cell pair axes schematic sketches. Z-axis (cyan) and XY-axis (purple) are perpendicular to each other and to the connecting axis between the cells' centers (black).
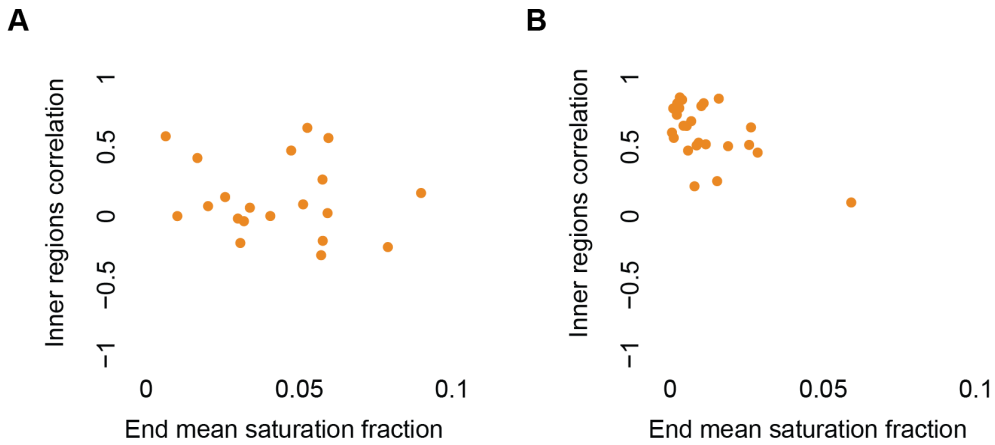
Figure S16: Association between inner regions correlations and the fraction of saturated pixels in the region used to measure cell-cell communication. For both panels, pair distances range between 4 and 10 cell diameters (60-150 μm, assuming mean fibroblast diameter of 15 μm). Correlations were calculated using the first derivative of fiber density dynamics. (**A**) Saturation-independent correlations along the connecting axis between the cells (Pearson correlation coefficient p-value > 0.05), N = 25 cell pairs. Image saturation does not hamper the ability to identify cell-ECM-cell communication along the dense fibrous band. (**B**) Image saturation reduces the ability to identify cell-ECM-cell communication 0.5 cell diameters (7.5 μm) above the connecting axis between the cells. N = 25 cell pairs, Pearson correlation coefficient = -0.58, p-value < 0.01.

Figure S17: Spatial decoupling of band formation and cell-ECM-cell communication in cell pairs with a visible band imaged in high temporal resolution of 5 minutes per frame. Pair distance of 60-150 μm. (**A**) Fiber density. Mean fiber density for systematic offsets in Z and XY axes. (**B**) Cell-ECM-cell communication. Mean fraction of higher "same", correlation between communicating pairs, versus "different", correlation between one cell from that pair and another cell from a different communicating pair for systematic offsets in Z and XY axes. Red 'x' marked that the null hypothesis that "same" - "different" correlations are distributed around zero was not rejected with p-value ≤ 0.05.
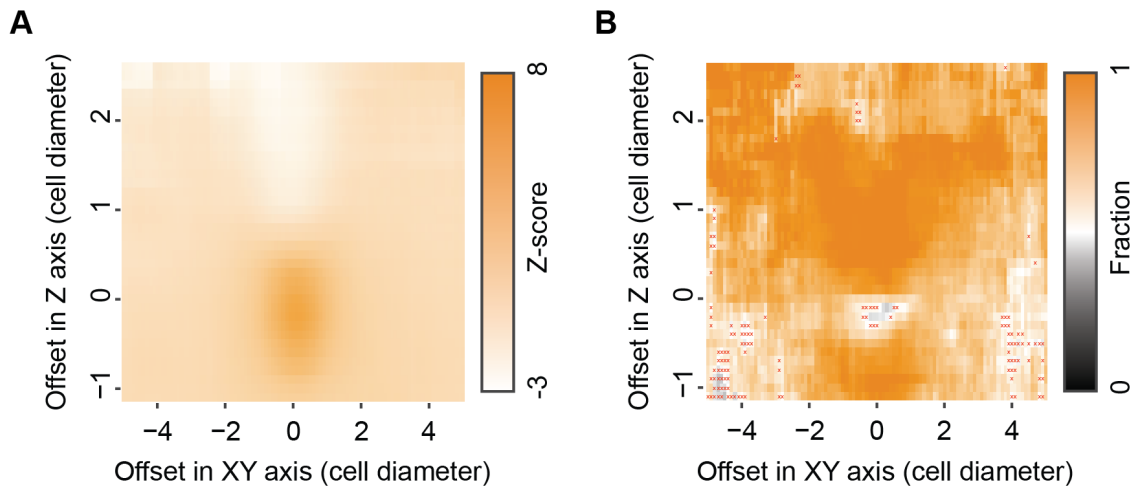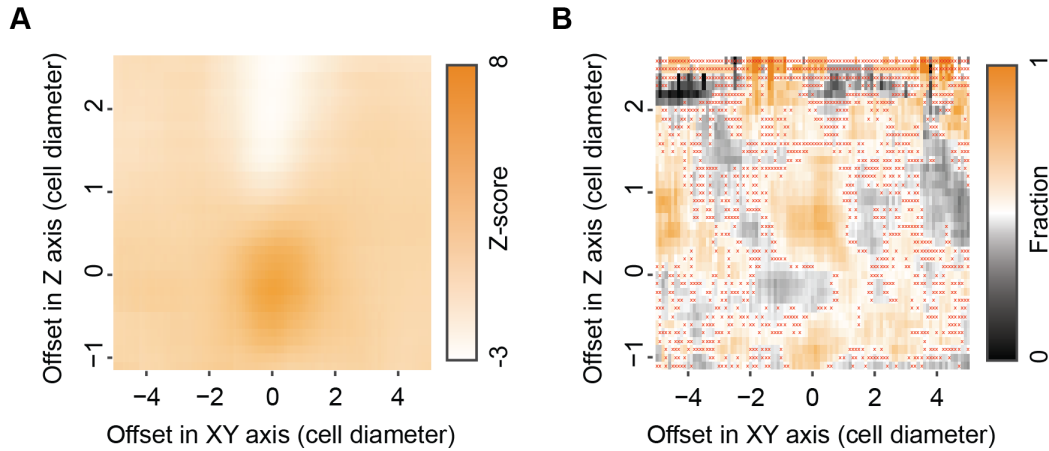
Figure S18: Spatial decoupling of band formation and cell-ECM-cell communication in pairs with no visible band imaged in high temporal resolution of 5 minutes. Pair distance of 60-150 μm. (**A**) Fiber density. Mean fiber density for systematic offsets in Z and XY axes. (**B**) Cell-ECM-cell communication. Mean fraction of higher "same", correlation between communicating pairs, versus "different", correlation between one cell from that pair and another cell from a different communicating pair for systematic offsets in Z and XY axes. Red 'x' marked that the null hypothesis that "Same" - "different" correlations are distributed around zero was not rejected with p-value ≤ 0.05.
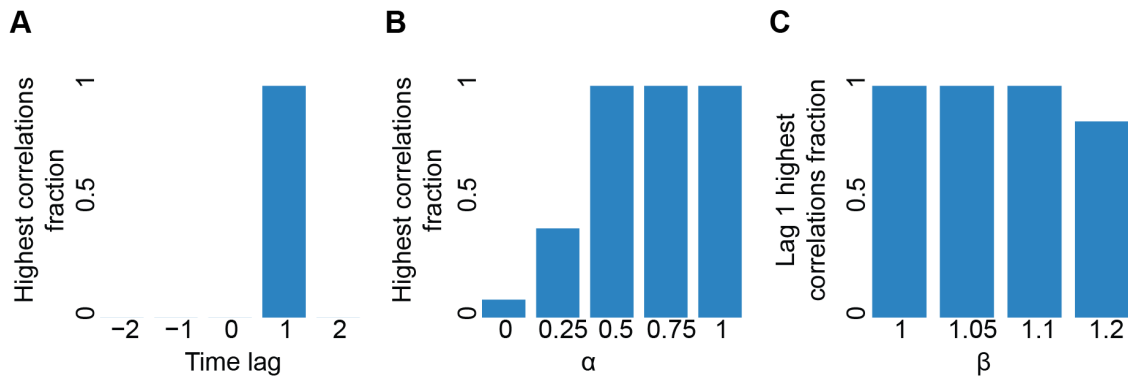
Figure S19: Leader-follower lag time analysis in simulated cell pairs. Inner cross correlation for different time lags. N = 13 cell pairs. Pairs distance = 7 cell diameters. The leader cell draws its contraction in each step independently from a normal distribution with mean of 1% and standard deviation of 0.5%. The follower cell draws its "intrinsic" component (contraction$_{follower}$) from the same distribution. The second derivative of the fiber density dynamics was used for correlation. Time lag is applied to the follower's time series before correlation is calculated. (**A**) Distribution of time lags that lead to maximal inner correlation. (**B**) Fraction of cell pairs where the simulated time lag (that was set to one step) leads to maximal inner correlation as a function of α values. Increased α implies an increased contribution of the extrinsic component - the influence by the leader cell. Note that α = 0 implies no leader effect and thus the fraction is expected to be random. (**C**) Fraction of cell pairs where the simulated time lag leads to maximal inner correlation as a function of β values. Increased β implies an increased contraction by the follower cell. α value was set to 1.
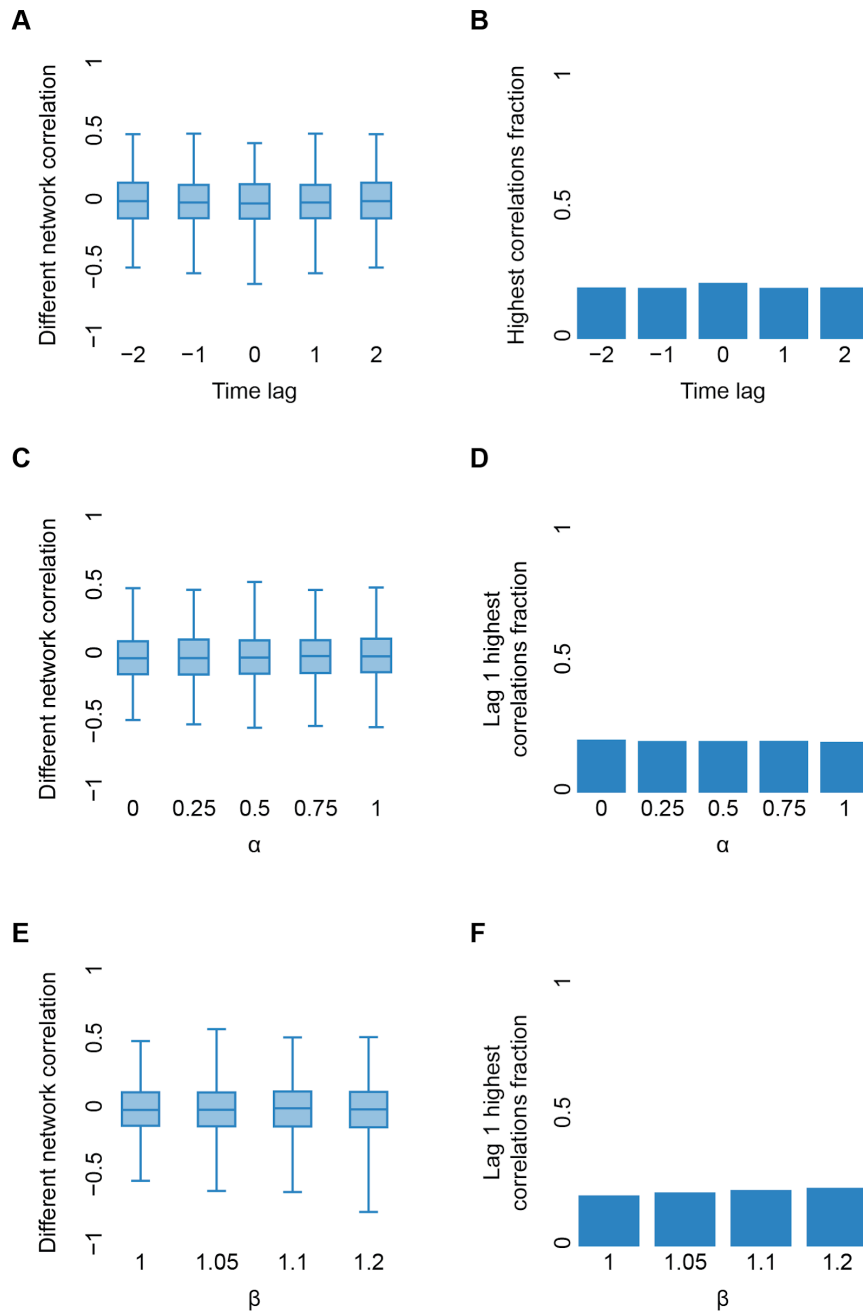
Figure S20: Cross correlation analysis of artificial pairing of simulated leader/follower cells that did not interact with one another as a control. Cross correlation for different time lags between a cell from one communicating pair and another cell from a different communicating pair. $N = 13$ cell pairs, pair distance = 7 cell diameters. The leader cell draws its contraction in each step independently from a normal distribution with mean of 1% and standard deviation of 0.5%. The follower cell draws its "intrinsic" component (contraction$_{follower}$) from the same distribution. The second derivative of the fiber density dynamics was used for correlation. The time lag is applied to the follower's time series before the correlation was calculated. (**A**) Distribution of correlations as a function of the time lag. (**B**) Distribution of time lags that lead to maximal correlation. (**C**) Distribution of the correlation for time lag = 1 as a

function of α values. Increased α implies an increased contribution of the extrinsic component for the communicating cell paris before the artificial pairing to cells that never communicated with one another. (**D**) Fraction of cell pairs where the simulated time lag (that was set to one step) leads to maximal correlation as a function of α values. (**E**) Distribution of the correlation for time lag = 1 as a function of β values. Increased β implies an increased contraction by the follower cell. α value was set to 1. (**F**) Fraction of cell pairs where the simulated time lag leads to maximal correlation as a function of β values.
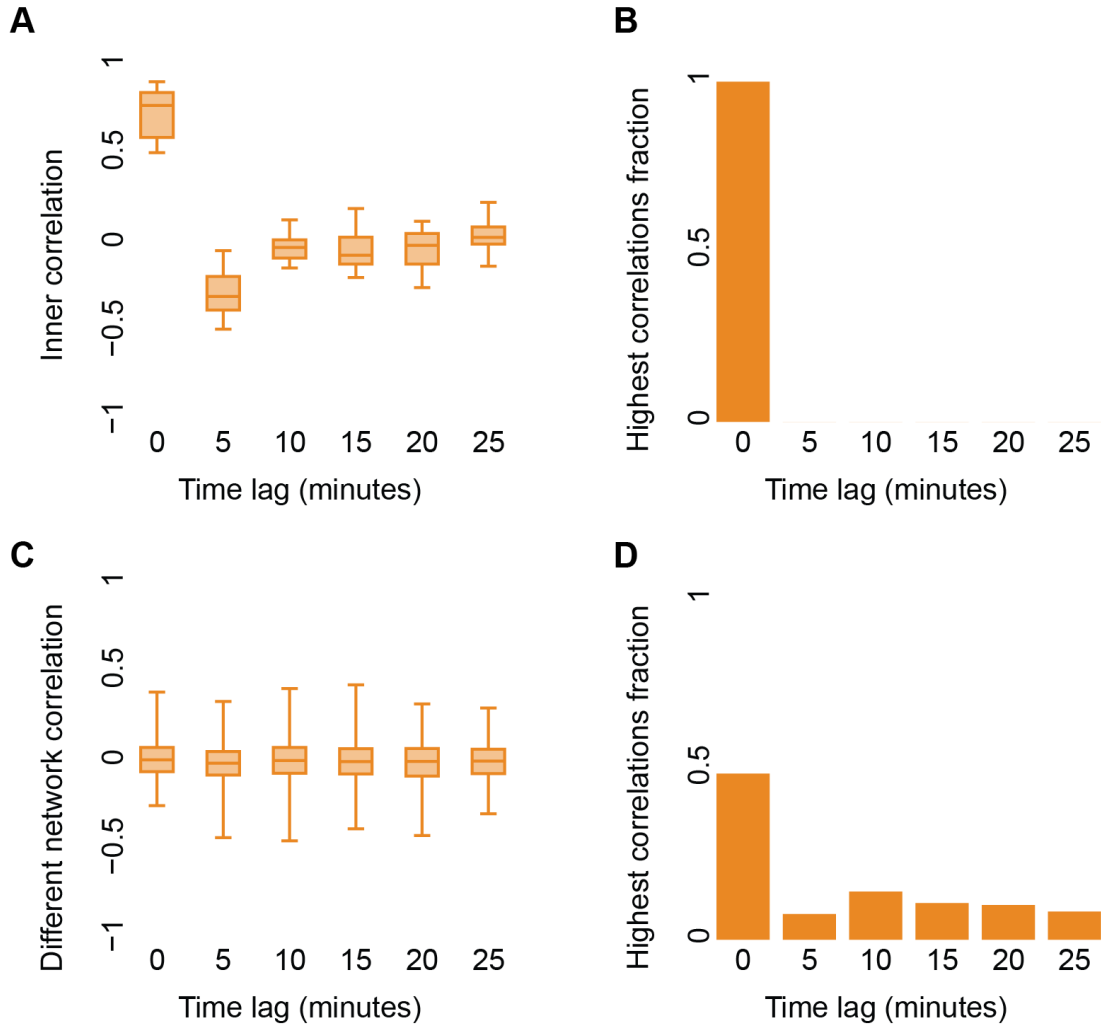
Figure S21: Cross correlation analysis did not identify leader-follower relations in experimental data. N = 19 communicating cell pairs with visible bands. Temporal resolution = 5 minutes between consecutive time frames. Pair distance of 60-150 μm. Quantification windows were placed 7.5 μm above the connecting axis between the cells (see Fig. 5E for schematics). Correlations were calculated using the first derivative of fiber density dynamics. Time lags were recorded with their absolute value (symmetry argument: no preference to a specific cell as in the simulations). (**A-B**) Inner cross correlation for different time lags. (**A**) Distribution of inner correlations as a function of the time lag. (**B**) Distribution of time lags that lead to maximal inner correlation. (**C-D**) Cross correlation for different time lags between one cell from a communicating pair and another cell from a different communicating pair as a control. (**C**) Distribution of correlations as a function of the time lag. (**D**) Distribution of time lags that lead to maximal correlation.
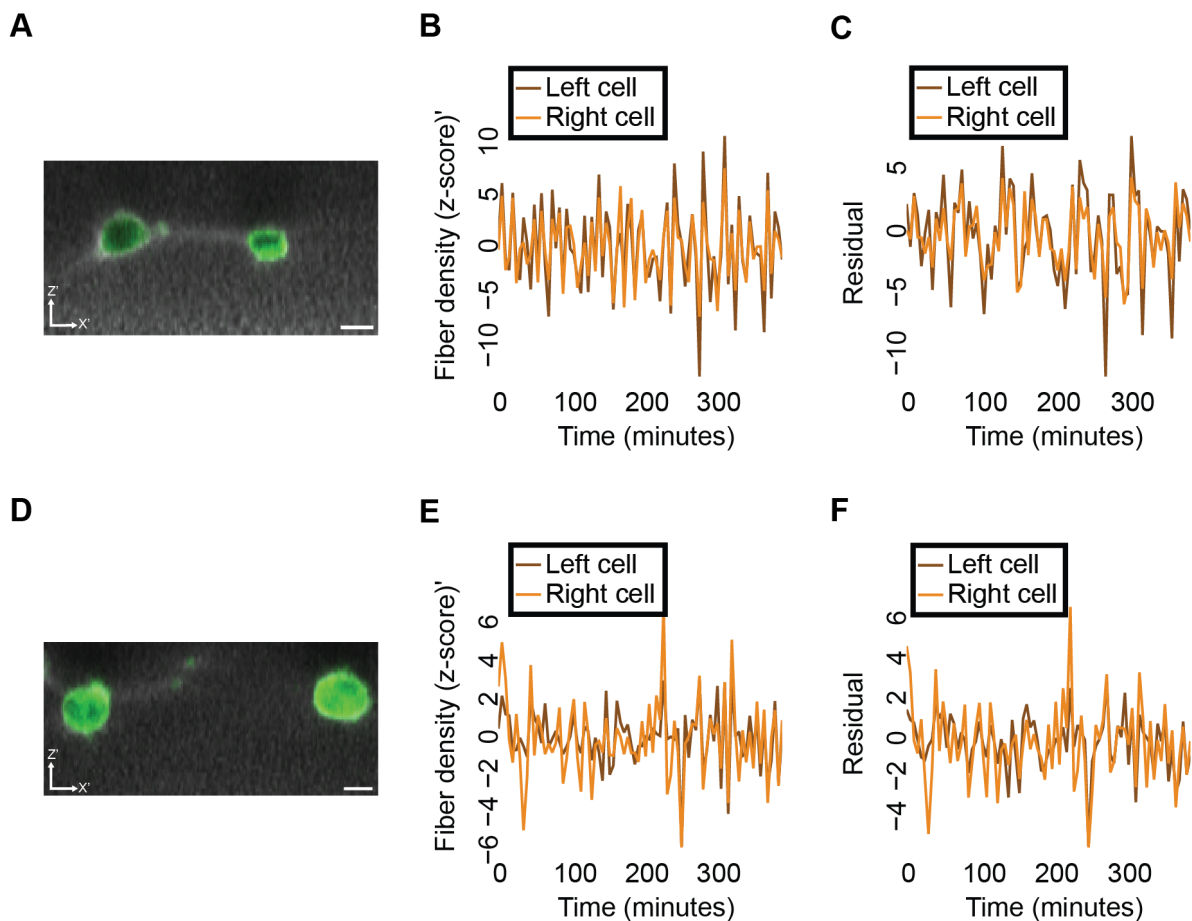
Figure S22: Identifying leaders and followers in experiments using Granger Causality (GC). Temporal resolution = 5 minutes. N = 73 cell pairs. Pairs distance 60-150 μm (~4-10 cell diameters). Quantification windows were placed 7.5 μm above the connecting axis between the cells. Granger causality was applied on the first derivative of fiber density dynamics. 21/73 of cell pairs (2/14 with visible band) passed a whiteness test for rejecting the null hypothesis regarding autocorrelation in the residuals (see Fig. S23). Five (one of which with a visible band, four of which without a visible band) out of these 21 cell pairs rejected the GC statistical test with p-value < 0.05. (**A-C**) One example of a leader (left) and follower (right) cell pair. GC p-value = 0.015 (FDR correction = 0.14). See also Video S11. (**A**) XY/Z projected snapshot after 400 minutes of live cell imaging. Scale bar = 15 μm. (**B**) Fiber density first derivative dynamics. (**C**) Residuals of the vector autoregression (VAR) model. (**D-F**) One example of a cell pair where cells are both leaders and followers. GC p-values = 0.009 (left is a leader, FDR correction = 0.13) and 0.005 (right is a leader, FDR correction = 0.1). See also Video S12. (**D**) XY/Z projected snapshot after 400 minutes of live cell imaging. Scale bar = 15 μm. (**E**) Fiber density first derivative dynamics. (**F**) Residuals of the VAR model.
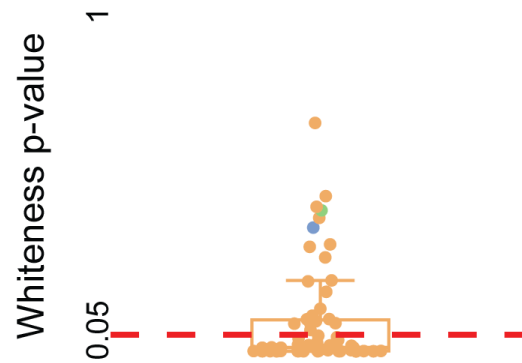
Figure S23: Residuals whiteness tests for vector autoregression (VAR) models based on experiment cell pairs dynamics. N = 73 cell pairs from N = 3 independent experiments. Temporal resolution = 5 minutes between consecutive time frames. Pairs distance of 60-150 μm. Quantification windows were placed 7.5 μm above the connecting axis between the cells (see Fig. 5E for schematics). Correlations were calculated using the first derivative of fiber density dynamics. Each data point shows the whiteness test p-value testing the null hypothesis of no autocorrelation in the residuals using Portmanteau test. The null hypothesis is not rejected for 21/73 of cell pairs (2/14 with visible band). The data point marked in green belongs to the cell pair presented in S22A-C. The data point marked in blue belongs to the cell pair presented in S22D-F.
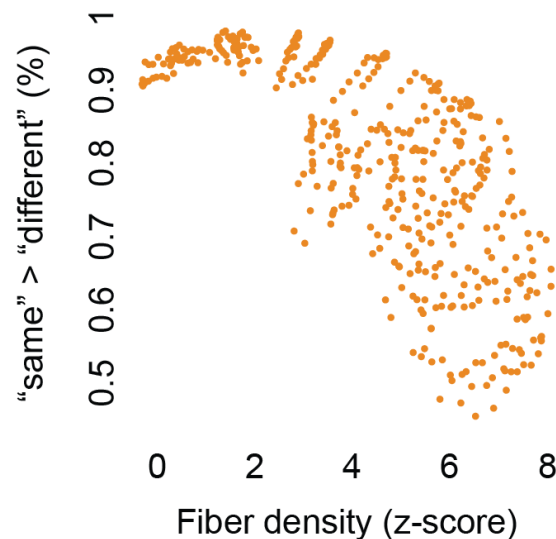
Figure S24: Association between fiber density and our ability to identify cell-ECM-cell communication with same-versus-different pair analysis. Each data point represents the mean fiber density in the quantification window (x-axis) and the fraction of cell pairs with "same" correlation higher than "different" correlation (y-axis) for different locations of the quantification window. The data here was derived from matched bins in Fig. 5B (x-axis) and Fig. 5C (y-axis) in a region that spans 1 cell diameter away from the quantification plane defined adjacent to the cells in the connecting axis between the communicating cells: all bins in the range -1≤XY≤1 and -1≤Z≤1. Pearson correlation coefficient = -0.73,

p-value < 0.0001. Note the stiff drop in cell-ECM-cell communication around fiber density of ~3-4 z-score.
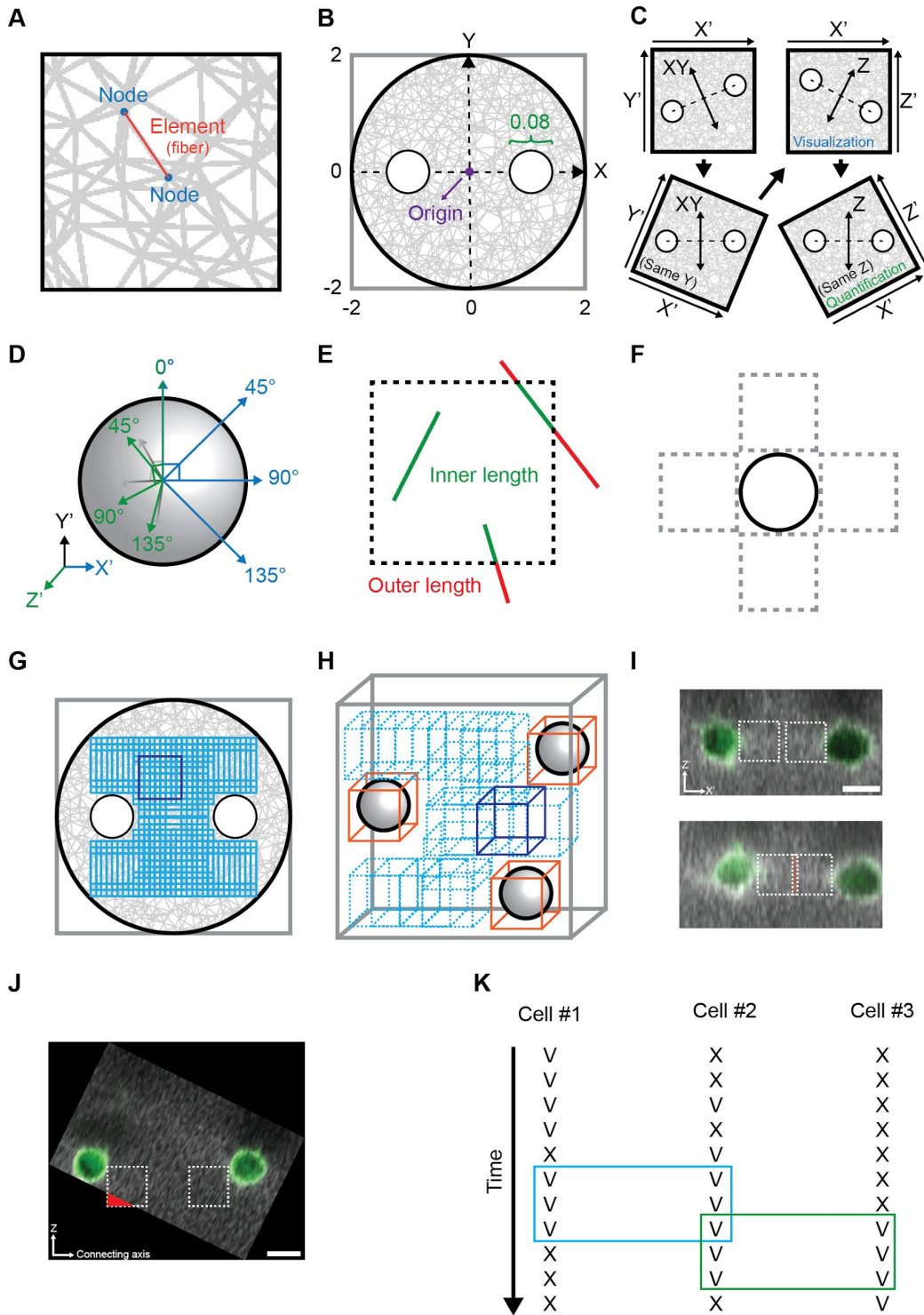
Figure S25: Methods. (**A**) Components of a finite-element simulation network. Fibers are represented by discrete one-dimensional elements (red) connected by two nodes (blue). (**B**) Finite-element network

dimensions. The simulated fibrous network was defined as a circular arena, of radius 2 AU, that is composed of connected elements. One or two circular voids, of radius 0.08 AU (green), define the cell/s. The center of the network is called the origin (purple). Single cells centers are located in the origin. Cell pairs centers are located along the X axis in predefined distance from the origin. Ratio of cell radius and the network radius in the depiction does not resemble the actual proportion between the two. (**C**) Transformation of cell pairs images. First transformation (top-left to bottom-left) aligns the cell centers to a common Y'-axis. Images are in top-view perspective. We use X' and Z' axes for cell pair visualization (top-right). The second transformation (top-right to bottom-right) aligns the cell centers to a common Z'-axis. Images are in side-view perspective. The transformed image (bottom-right) is used for cell pair quantification. (**D**) Transformation of single cell images. Illustration is in top-view perspective. First transformation (blue) in 0°, 45°, 90° or 135° in the XY axis. Second transformation (green) in 0°, 45°, 90° or 135° in the Z' axis. (**E**) Quantifying fiber (simulation elements) intersection with the quantification windows in simulations. The quantification window is illustrated with a dashed box. To be considered, a fiber must be either exclusively inside the quantification window or crossing the window's boundaries. The sub-fiber within the window's boundaries (green) are included while sub-fibers external to the quantification window (red) are excluded from the quantification. (**F**) The quantification windows for simulated single cells are placed in four directions at 90 degrees radial intervals. (**G**) Quantification windows in simulations used for computing the normalization parameters. Quantification window (blue as an example) is the size of a cell diameter by a cell diameter (0.08 x 0.08 AU). All quantification windows used for this computation (cyan) are located inside the network boundaries and outside the cells with a step resolution (overlap) of 0.02 (AU) in each of the axes. (**H**) Quantification windows in experiments used for computing the normalization parameters. Quantification window (blue as an example) length is 15 μm, approximately the cell diameter in 3D. All quantification windows used for this computation (cyan) are located exclusively inside the image boundaries in all axes and without intersection with bounding boxes (orange) around the cells, with a step resolution (overlap) of 1/10 of the image axis length for each axis. (**I**) An example of overlapping quantification windows between a pair of communicating cells. Images are in a side-view average projection perspective. Quantification windows are marked in white dashed boxes. At the onset of imaging (top) the quantification did not overlap, however after 3.5 hours of live cell imaging (bottom) the quantification windows did overlap (orange area). Scale bar = 15 μm. (**J**) An example of a quantification window extending beyond the image boundaries at the onset of imaging. Image is in a side-view perspective with averaged pixel intensities visualization after the transformation. Quantification windows are marked in white dashed boxes. Red area represents the sub-window outside the image boundaries. Scale bar = 15 μm. (**K**) Valid ("V") and invalid ("X") quantification windows (see Methods for definition) over time of three different cells. Blue rectangle represents the longest shared valid temporal sequence for cell #1 and cell #2 and the green rectangle for cell #2 and cell #3.

Supplementary tables legends

Table S1: Simulated and experimental data tables. Each data information is presented in a different sheet. Simulations include single cells and cell pairs, heterogeneity and leader / follower in pair distances 5, 7 and 9 cell diameters. Experiments include single cells and cell pairs in low (N = 1 experiment) and high (N = 3 experiments) temporal resolutions of real, "fake-static" and "fake-following" types of cell pairs, with or without a band, in pair distances 4-6, 6-8 and 8-10 cell diameters.

Supplementary video legends

Video S1: 3D representation of a cell pair quantification axes. Microscopy axes in the left bottom corner: X' (dark green), Y' (orange) and Z' (cyan). Cells (green) are in different Z' coordinates. Connecting axis (black) is between the cell's centers. Quantification windows (yellow) are adjacent to each cell along the connecting axis (black) between the cell's centers, left and right sides are parallel to the microscopy axial plane. The Z-axis (cyan) and the XY-axis (purple) are perpendicular to each other and to the connecting axis (black). The video demonstrates offsets between -1 and 1 cell diameters of the quantification windows in the Z (cyan) and XY (purple) axes.

Video S2: Finite-element simulation of a single cell contracting in a 2D fibrous network. Cell contracts 1% for 50 steps (Methods).

Video S3: Time-lapse confocal imaging of a single fibroblast embedded in a 3D fibrin gel. XY/Z average projection visualization of a single cell (Methods). Time resolution: 21 minutes. Scale bar = 15 μm.

Video S4: Finite-element simulation of a cell pair contracting in a 2D fibrous network. Pair distance = 7 cell diameters. Both cell contracts 1% for 50 steps (Methods).

Video S5: Time-lapse confocal imaging of a pair of fibroblast cells embedded in a 3D fibrin gel forming a band of dense fibers in the connecting axis between the cells. XY/Z average projection visualization of a pair of cells (Methods). Pair distance: 117 μm. Time resolution: 15 minutes. Scale bar = 15 μm.

Video S6: Cell heterogeneity is necessary to distinguish between matched inner and outer correlations. See Fig. 3D-E for statistics.

Video S7: Pairs distance effect on the quantification and distinguishability of matched inner and outer regions. See Fig. S6 for details and statistics.

Video S8: Window distance effect on the quantification and distinguishability of matched inner and outer regions. See Fig. S7 for details and statistics.

Video S9: Time-lapse confocal imaging of a pair of fibroblast cells embedded in 3D fibrin gel not forming a band of dense fibers in the connecting axis between the cells. Pair distance: 110 μm. Time resolution: 15 minutes. Scale bar = 15 μm.

Video S10: Matchmaking between communication partners. Images are in a side-view perspective. Cell pairs are with visible bands. Quantification windows (white dashed rectangles) are adjacent to each cell along the connecting axis (black) between the cell's centers. The video demonstrates the analysis of a cell by correlating it's ECM remodeling dynamics with all other candidates. Correlation results are for demonstration purpose only.

Video S11: Time lapse imaging of leader (left) and follower (right) cells identified by Granger Causality. Full analysis in Fig. S22A-C.

Video S12: Time lapse imaging of a cell pair where Granger Causality was identified in both directions. Full analysis in Fig. S22D-F.

Video S13: Time lapse imaging of a cell pair with a manually identified illumination artifact in several time frames that were excluded from analysis.

References

1. Benham-Pyle, B. W., Pruitt, B. L. & Nelson, W. J. Cell adhesion. Mechanical strain induces E-cadherin-dependent Yap1 and β-catenin activation to drive cell cycle entry. *Science* **348**, 1024–1027 (2015).

2. Evans, W. H. & Martin, P. E. M. Gap junctions: structure and function (Review). *Mol. Membr. Biol.* **19**, 121–136 (2002).

3. Rustom, A., Saffrich, R., Markovic, I., Walther, P. & Gerdes, H.-H. Nanotubular highways for intercellular organelle transport. *Science* **303**, 1007–1010 (2004).

4. Yáñez-Mó, M. *et al.* Biological properties of extracellular vesicles and their physiological functions. *J. Extracell. Vesicles* **4**, 27066 (2015).

5. Reinhart-King, C. A., Dembo, M. & Hammer, D. A. Cell-cell mechanical communication through compliant substrates. *Biophys. J.* **95**, 6044–6051 (2008).

6. Nitsan, I., Drori, S., Lewis, Y. E., Cohen, S. & Tzlil, S. Mechanical communication in cardiac cell synchronized beating. *Nat. Phys.* **12**, 472–477 (2016).

7. Kim, J. *et al.* Stress-induced plasticity of dynamic collagen networks. *Nat. Commun.* **8**, 842 (2017).

8. Shi, Q. *et al.* Rapid disorganization of mechanically interacting systems of mammary acini. *Proc. Natl. Acad. Sci. U. S. A.* **111**, 658–663 (2014).

9. Ban, E. *et al.* Mechanisms of Plastic Deformation in Collagen Networks Induced by Cellular Forces. *Biophys. J.* **114**, 450–461 (2018).

10. Notbohm, J., Lesman, A., Rosakis, P., Tirrell, D. A. & Ravichandran, G. Microbuckling of fibrin provides a mechanism for cell mechanosensing. *J. R. Soc. Interface* **12**, 20150320 (2015).

11. Goren, S., Koren, Y., Xu, X. & Lesman, A. Elastic Anisotropy Governs the Range of Cell-Induced Displacements. *Biophys. J.* **118**, 1152–1164 (2020).

12. Ronceray, P., Broedersz, C. P. & Lenz, M. Fiber networks amplify active stress. *Proc. Natl. Acad. Sci. U. S. A.* **113**, 2827–2832 (2016).

13. Ma, X. *et al.* Fibers in the extracellular matrix enable long-range stress transmission between cells. *Biophys. J.* **104**, 1410–1418 (2013).

14. Korff, T. & Augustin, H. G. Tensional forces in fibrillar extracellular matrices control directional capillary sprouting. *J. Cell Sci.* **112 (Pt 19)**, 3249–3258 (1999).

15. Natan, S., Koren, Y., Shelah, O., Goren, S. & Lesman, A. Long-range mechanical coupling of cells in 3D fibrin gels. *Mol. Biol. Cell* **31**, 1474–1485 (2020).

16. Winer, J. P., Oake, S. & Janmey, P. A. Non-linear elasticity of extracellular matrices enables contractile cells to communicate local position and orientation. *PloS One* **4**, e6382 (2009).

17. Han, Y. L. *et al.* Cell contraction induces long-ranged stress stiffening in the extracellular matrix. *Proc. Natl. Acad. Sci. U. S. A.* **115**, 4075–4080 (2018).

18. Doyle, A. D. & Yamada, K. M. Mechanosensing via cell-matrix adhesions in 3D microenvironments. *Exp. Cell Res.* **343**, 60–66 (2016).

19. Pakshir, P. *et al.* Dynamic fibroblast contractions attract remote macrophages in fibrillar collagen matrix. *Nat. Commun.* **10**, 1850 (2019).

20. Stopak, D. & Harris, A. K. Connective tissue morphogenesis by fibroblast traction. I. Tissue culture observations. *Dev. Biol.* **90**, 383–398 (1982).

21. Davis, G. E. & Camarillo, C. W. Regulation of endothelial cell morphogenesis by integrins, mechanical forces, and matrix guidance pathways. *Exp. Cell Res.* **216**, 113–123 (1995).

22. Guo, C.-L. *et al.* Long-range mechanical force enables self-assembly of epithelial tubular patterns. *Proc. Natl. Acad. Sci. U. S. A.* **109**, 5576–5582 (2012).

23. Wells, R. G. Tissue mechanics and fibrosis. *Biochim. Biophys. Acta* **1832**, 884–890 (2013).

24. Duscher, D. *et al.* Mechanotransduction and fibrosis. *J. Biomech.* **47**, 1997–2005 (2014).

25. Han, W. *et al.* Oriented collagen fibers direct tumor cell intravasation. *Proc. Natl. Acad. Sci. U. S. A.* **113**, 11208–11213 (2016).

26. Ahmadzadeh, H. *et al.* Modeling the two-way feedback between contractility and matrix realignment reveals a nonlinear mode of cancer cell invasion. *Proc. Natl. Acad. Sci. U. S. A.* **114**, E1617–E1626 (2017).

27. Cohen, O. & Safran, S. A. Theory of frequency response of mechanically driven cardiomyocytes. *Sci. Rep.* **8**, 2237 (2018).

28. Zemel, A. & Kemkemer, R. Cell–Matrix and Cell–Cell Mechanical Interactions. in *Cell and Matrix Mechanics* 136–165 (CRC Press, 2014).

29. Wang, H., Abhilash, A. S., Chen, C. S., Wells, R. G. & Shenoy, V. B. Long-range force transmission in fibrous matrices enabled by tension-driven alignment of fibers. *Biophys. J.* **107**, 2592–2603 (2014).

30. Clark, A. G. *et al.* Viscoelastic relaxation of collagen networks provides a self-generated directional cue during collective migration. *bioRxiv* 2020.07.11.198739 (2020) doi:10.1101/2020.07.11.198739.

31. Mark, C. *et al.* Collective forces of tumor spheroids in three-dimensional biopolymer networks. *eLife* **9**, (2020).

32. Granger, C. W. J. Econometrica: Journal of the Econometric Society. *JSTOR* **37**, 424 (1969).

33. Benjamini, Y. & Hochberg, Y. Controlling the false discovery rate: a practical and powerful approach to multiple testing. *J. R. Stat. Soc. Ser. B Methodol.* **57**, 289–300 (1995).

34. Cohen, O. & Safran, S. A. Elastic interactions synchronize beating in cardiomyocytes. *Soft Matter* **12**, 6088–6095 (2016).

35. Hall, M. S. *et al.* Fibrous nonlinear elasticity enables positive mechanical feedback between cells and ECMs. *Proc. Natl. Acad. Sci. U. S. A.* **113**, 14043–14048 (2016).

36. Machacek, M. *et al.* Coordination of Rho GTPase activities during cell protrusion. *Nature* **461**, 99–103 (2009).

37. Discher, D. E., Janmey, P. & Wang, Y.-L. Tissue cells feel and respond to the stiffness of their substrate. *Science* **310**, 1139–1143 (2005).

38. Ma, B. *et al.* Cell Painting, a high-content image-based assay for morphological profiling using multiplexed fluorescent dyes. *Nat. Protoc.* **11**, 1757–1774 (2016).

39. McQuin, C. *et al.* CellProfiler 3.0: Next-generation image processing for biology. *PLoS Biol.* **16**, e2005970 (2018).

40. Edmondson, R., Broglie, J. J., Adcock, A. F. & Yang, L. Three-dimensional cell culture systems and their applications in drug discovery and cell-based biosensors. *Assay Drug Dev. Technol.* **12**, 207–218 (2014).

41. Desai, S. S. *et al.* Physiological ranges of matrix rigidity modulate primary mouse hepatocyte function in part through hepatocyte nuclear factor 4 alpha. *Hepatol. Baltim. Md* **64**, 261–275 (2016).

42. Conklin, M. W. *et al.* Aligned collagen is a prognostic signature for survival in human breast carcinoma. *Am. J. Pathol.* **178**, 1221–1232 (2011).

43. Mann, A. *et al.* Force chains in cell-cell mechanical communication. *J. R. Soc. Interface* **16**, 20190348 (2019).

44. Sopher, R. S. *et al.* Nonlinear Elasticity of the ECM Fibers Facilitates Efficient Intercellular Communication. *Biophys. J.* **115**, 1357–1370 (2018).

45. Stevens, M. M. & George, J. H. Exploring and engineering the cell surface interface. *Science* **310**, 1135–1138 (2005).

46. Wade, R. J. & Burdick, J. A. Engineering ECM signals into biomaterials. *Mater. Today* **15**, 454–459 (2012).

47. Kang, H. *et al.* Nonlinear elasticity of stiff filament networks: strain stiffening, negative normal stress, and filament alignment in fibrin gels. *J. Phys. Chem. B* **113**, 3799–3805 (2009).

48. Liang, L., Jones, C., Chen, S., Sun, B. & Jiao, Y. Heterogeneous force network in 3D cellularized collagen networks. *Phys. Biol.* **13**, 066001 (2016).

49. Cordelières, F. P. & Jackson, J. 3D objects counter. *ImageJ Image Process.* (2005).

50. Vader, D., Kabla, A., Weitz, D. & Mahadevan, L. Strain-induced alignment in collagen gels. *PloS One* **4**, e5902 (2009).

51. Kwiatkowski, D., Phillips, P. C. B., Schmidt, P. & Shin, Y. Testing the null hypothesis of stationarity against the alternative of a unit root: How sure are we that economic time series have a unit root? *J. Econom.* **54**, 159–178 (1992).

52. Cheung, Y.-W. & Lai, K. S. Lag order and critical values of the augmented Dickey–Fuller test. *J. Bus. Econ. Stat.* **13**, 277–280 (1995).

53. Granger, C. W. J. Investigating Causal Relations by Econometric Models and Cross-spectral Methods. *Econometrica* **37**, 424–438 (1969).

54. Seabold, S. & Perktold, J. Statsmodels: Econometric and statistical modeling with python. in *Proceedings of the 9th Python in Science Conference* vol. 57 61 (Austin, TX, 2010).

55. Lütkepohl, H. *New introduction to multiple time series analysis*. (Springer Science & Business Media, 2005).

תקציר

תאים ביולוגיים חשים, מפעילים ומגיבים לתכונות המכניות של הסביבה הקרובה שלהם במגוון רחב של תהליכים פיזיולוגיים, אך עם זאת תשובות לשאלות האם וכיצד תאים מפרשים רמזים סביבתיים על מנת לתקשר עם תאים מרוחקים לרוב עדיין לא קיבלו מענה. במחקר זה אנו מציגים שיטה חישובית להסקה וכימות התקשורת המכנית ארוכת הטווח בין תאים דרך המטריצה החוץ-תאית (המוגדרת להיות תקשורת תא-סביבה-תא). מצאנו כי התנודות בעיצוב מחדש של המטריצה החוץ-תאית המקומית הנמצאת בין תאים מתקשרים מסונכרנות בעקבות כוחות המועברים בין התאים. באמצעות מתאם תנודות אלו, בהדמיות מחשב ובניסויי צילום תלת-ממדים מתמשכים של תאים סיביים המוטמעים בחומר ג'ל סיבי, השיטה שאנו מציגים התאימה בדיוק גבוה בין זוגות תאים מתקשרים, וזיהתה האם ובאיזה היקף תא מסוים הושפע מבן זוגו איתו תיקשר. באמצעות שיטה זו, גילינו כי תאים מגיבים באופן פעיל לאות המכני שהם מרגישים מהתא האחר, ומעצימים את היווצרותה של רצועת סיבים צפופה בין התאים המתקשרים. שיטה זו מכשירה את הקרקע למדידת ההיבטים הבסיסיים של תקשורת בין-תאית מכנית ארוכת טווח בהקשרים פיזיולוגיים ועשויה לספק היצג נתונים שימושי עבור מידע רב מבוסס צילום ניסויי תלת-ממדי.

אוניברסיטת בן-גוריון בנגב
הפקולטה למדעי ההנדסה
המחלקה **להנדסת תוכנה ומערכות מידע**

כימות התקשורת המכנית ארוכת הטווח של תא-תא

חיבור זה מהווה חלק מהדרישות לקבלת תואר "מגיסטר" בהנדסה

מאת: אסף נחום

מנחה: ד"ר אסף זריצסקי

חתימת המחבר: .... תאריך:............18/09/20

חתימת המנחה:.. . תאריך:............19/09/20

חתימת יו"ר ועדת תואר שני מחלקתית.................................... תאריך:..

אלול תש"פ
ספטמבר 2020

אוניברסיטת בן-גוריון בנגב

הפקולטה למדעי ההנדסה

המחלקה **להנדסת תוכנה ומערכות מידע**

כימות התקשורת המכנית ארוכת הטווח של תא-תא

חיבור זה מהווה חלק מהדרישות לקבלת תואר "מגיסטר" בהנדסה

מאת: אסף נחום

אלול תש"פ　　　　　　　　　　　　　　　　　　ספטמבר 2020